Regulatory T cells attenuate chronic inflammation and cardiac fibrosis in hypertrophic cardiomyopathy

Ying-Jie Wang[1,2]*, Kamayani Singh[1,2], Adam B. Lokman[3], Siwei Deng[1,2], Balaraju Sunitha[1,2], Jose Coelho Lima Junior[4], Julia Beglov[1,2], Matthew Kelly[1,2], Andrew Blease[1,2], Jacky CK Fung[1,2], Anan Huang[1,2], Moustafa Attar[5], Lee-Anne Stork[6], Mahon L. Maguire[7], Jürgen E. Schneider[8], Steve B. Marston[9], Elizabeth J. Soilleux[10], Calliope A. Dendrou[5], Mark Coles[5], Christopher D. Buckley[5], Jonathan G. Seidman[12], Christine E. Seidman[12, 13], Charles Redwood[1], Houman Ashrafian[1,2,11], Hugh Watkins[1,2,11]*

1. Division of Cardiovascular Medicine, Radcliffe Department of Medicine, University of Oxford, Oxford, OX3 9DU, United Kingdom.
2. Centre for Human Genetics, University of Oxford, Oxford, OX3 7BN, United Kingdom.
3. Institute of Developmental and Regenerative Medicine, University of Oxford, Oxford, OX3 7TY, United Kingdom.
4. Division of Cellular and Molecular Pathology, Addenbrooke's Hospital, Cambridge, CB2 0QQ, United Kingdom.
5. Kennedy Institute of Rheumatology, University of Oxford, Oxford, OX3 7FY, United Kingdom.
6. RDM Clinical Laboratory Sciences, John Radcliffe Hospital, Oxford, OX3 9DU, United Kingdom.
7. Centre for Preclinical Imaging, University of Liverpool, Liverpool, L69 3BX, United Kingdom.
8. Leeds Institute of Cardiovascular and Metabolic Medicine, University of Leeds, LS2 9NL, United Kingdom.
9. Faculty of Medicine, National Heart & Lung Institute, Imperial College London, SW3 6LY, United Kingdom.
10. Department of Pathology, University of Cambridge, Cambridge, CB2 1QP, United Kingdom.
11. Experimental Therapeutics, Radcliffe Department of Medicine, University of Oxford, Oxford, OX3 9DU, United Kingdom.
12. Department of Genetics, Harvard Medical School, Boston, MA 02115, USA
13. Division of Cardiovascular Medicine, Brigham and Women's Hospital, Boston, Massachusetts, MA 02115, USA

*Correspondence should be addressed to: Hugh.Watkins@rdm.ox.ac.uk ; Ying-Jie.Wang@cardiov.ox.ac.uk

OVERLINE:

One Sentence Summary:

Regulatory T cells mitigate cardiac fibrosis and dysfunction in familial hypertrophic cardiomyopathy by modulating chronic inflammation.

Editor's summary:

Abstract

Hypertrophic cardiomyopathy (HCM) is a common, serious, genetic heart muscle disorder. Although the biophysical mechanisms by which gene variants in sarcomeric proteins disrupt cardiomyocyte function are largely understood, the cellular and molecular pathways leading to the complex, variable and adverse remodeling of the non-myocyte compartment are unexplained. Here we report that post-mortem and explanted human HCM hearts exhibited chronic focal leukocyte infiltration and prominent activation of immune cells. Gene set enrichment analysis (GSEA) revealed that active immune responses were present in the mid- and late-stage HCM human hearts and in mouse hearts from several HCM mouse models. The alpha actin cardiac 1-E99K (*Actc1*$^{\mathrm{E99K}}$) HCM mouse model was selected for the study because it closely recapitulates the features of progressive remodeling and fibrosis seen in advanced disease in patients. Genetic depletion of lymphocytes in recombination activating gene 1 – knockout (*Rag-1*$^{\mathrm{KO}}$) mice led to marked exacerbation of adverse cardiac remodeling in the *Actc1*$^{\mathrm{E99K}}$ mice. Detailed characterization of cardiac regulatory T cells (Tregs) demonstrated a time-dependent increase in *Actc1*$^{\mathrm{E99K}}$ hearts with altered immunosuppressive profiles. Adoptive transfer of splenic Tregs reduced cardiac fibrosis and improved systolic dysfunction in *Actc1*$^{\mathrm{E99K}}$ mice with or without lymphocytes. In addition, low dose interleukin-2 (IL-2)/anti-IL-2 complex (IL-2/c), which specifically induced Treg expansion in vivo, significantly ameliorated cardiac fibrosis and reduced macrophage infiltration and activation in *Actc1*$^{\mathrm{E99K}}$ mice. These data contribute to our understanding of HCM and support the use of Tregs as a clinically testable therapeutic strategy for cardiac fibrosis in the HCM heart.

INTRODUCTION

Familial hypertrophic cardiomyopathy (HCM) is an autosomal dominant disease characterized by unexplained hypertrophy of the ventricle, myocyte disarray, and fibrosis (*1, 2*). Although often asymptomatic, HCM can cause sudden cardiac death (SCD) in the young and a high burden of heart failure in later life (*3, 4*). The discovery of sarcomere mutations has shed light on the cause of the disease (*5-7*). Hundreds of HCM-causing mutations in nine principal sarcomeric genes have been identified during the last three decades. Affected individuals are heterozygous, with a single pathogenic variant causing their cardiomyopathy. Thus it is now understood that pathogenic variants in sarcomere protein genes that evoke hypercontractility, poor relaxation, and increased energy demand by the heart, are the predominant cause of familial HCM (*8-12*). Although sarcomeric mutations and their biophysical consequences for the cardiomyocyte are clearly key initiators of the disease, downstream events in the non-cardiomyocyte compartment of the heart are very likely to be responsible for many important aspects of the disease phenotype (*13-15*). HCM is characterized by progressive tissue remodeling with prominent interstitial and focal fibrosis (*16, 17*). This is a major contributor to the mechanical dysfunction seen in advanced stages of HCM, and measures of myocardial scar burden by magnetic resonance imaging (MRI) are strong predictors of adverse outcome (*18, 19*). In a subset of patients, this remodeling leads to a ‘burned out’ stage of HCM with declining contractility and a very poor outlook (*20, 21*). Understanding the drivers of the remodeling process in HCM will be important for future strategies for disease-modifying therapies. Current approaches, including allosteric myosin modulators (*22*) and approaches to correct the underlying genetic defects (*23, 24*), will only address cardiomyocyte dysfunction; without therapy to halt or reverse fibrosis, functional improvement in established disease is likely to be limited.

Among the diverse cell types in the non-cardiomyocyte compartment of the heart, a promising candidate contributing to this remodeling is the immune cell. Immune cells often work to maintain organ homeostasis (repair and regeneration) at tissue barriers such as the lung, gut, and skin. However, immune cells may also have maladaptive consequences for cardiac homeostasis. As an illustration, cardiac macrophages serve as ‘scavengers’ clearing whole or components of injured cells by its surface receptor MER Proto-Oncogene, Tyrosine Kinase (MERTK) (*25*) or 'conductors' through their physical contact with pace-maker cells by Connexin 43 at the atrioventricular (AV) node to maintain cardiac rhythm (*26*). In other circumstances, pro-fibrotic and pro-inflammatory macrophages may infiltrate myocardial tissue and exacerbate cardiac injury (*27*). Similarly, lymphocytes may also have diverse and divergent roles in cardiac diseases. T cells are thought to be detrimental in autoimmune myocarditis (*28*) and heart failure (*29*). Tregs, on the other hand, are potent suppressors of the immune response, driving immune tolerance and suppressing unwanted inflammation (*30*). Unlike other cardiac disorders where inflammation is known to play a role, relatively little is known about the immune landscape and immune response in HCM. Low grade inflammation has been reported in patients with an HCM-causing mutation D175N in the α-tropomyosin gene (*31*). Recent single nucleus RNA-seq studies confirmed the existence of various immune cells in the heart (*32, 33*).

Here we demonstrate focal infiltration of immune cells, and active immune responses, in late-stage HCM human hearts. Similar features were seen in four different HCM mouse models using gene set enrichment analysis (GSEA) and Pathway RespOnsive GENes (PROGENy) analysis (*34*). Among those models, we employ the cardiac actin *Actc1*$^{\mathrm{E99K}}$ HCM mouse model that reproduces not only common pathogenic features, such as higher calcium sensitivity and actin-activated adenosine triphosphatase (ATPase) activity, seen in HCM caused by other sarcomeric gene mutations, but also apical fibrosis and prominent remodeling processes that are notable features in human subjects bearing the same gene variant. Similar findings were confirmed in the *Actc1*$^{\mathrm{E99K}}$ HCM mouse and late-stage human HCM hearts, including adverse tissue remodeling and fibrosis, cardiac dysfunction, immune cell infiltration, and an RNA signature of upregulated immune response pathways. We therefore went on to perform longitudinal and intervention studies to understand the role of immune response in adverse remodeling using the HCM mouse model.

RESULTS

Focal infiltration and chronic inflammation in human HCM hearts

To investigate the frequency, pattern, and degree of immune cell infiltration in a broad set of patients with HCM, and to compare these with normal heart failure and myocarditis hearts, we screened 39 post-mortem or explant heart samples using immunohistochemistry. The baseline characteristics of selected cases are documented in table S1. All cases of HCM showed increased heart weight with associated fibrosis (table S1) whereas most cases of myocarditis showed no change in heart weight and fibrosis when compared to controls with similar body mass index (BMI). Immune cells, including $CD3^+$ T cells, $CD11b^+$ myeloid cells, and $CD68^+$ macrophages, were present in clusters in both the epicardium and mid-wall of most of the HCM and myocarditis cases but not in heart failure cases (Fig. 1, A to C). Although there were fewer infiltrating immune cells in HCM than those in myocarditis cases, a significant increase (two to four fold) was noticeable in HCM hearts when compared to healthy controls (Fig. 1, D to F).

To investigate immune cell activation in human HCM hearts, we performed GSEA on publicly available single-nucleus RNA sequencing (snRNA) data. This included tissue from septal myectomy in patients with obstructive HCM (mid-stage disease with high contractility) and explants from healthy donors (*33*), as well as left ventricle samples from end-stage failing HCM hearts and non-failing controls (*32*). In myectomy samples, GSEA revealed upregulation of extracellular matrix remodeling and immunological pathways in non-cardiomyocytes (Fig. 1G). End-stage failing HCM hearts showed downregulation of oxidative phosphorylation and significant alterations in fibrotic and immunological pathways across multiple cell types, including cardiomyocytes (Fig. 1G). Several hallmark gene sets (*35*) were significantly enriched in immune cells from failing HCM hearts. These gene sets or pathways, including Interferon-alpha and -gamma (IFN-α and IFN-γ) responses, tumor necrosis factor-alpha (TNF-α) Signaling By nuclear factor kappa B (NFκB), Allograft Rejection, Inflammatory Response, and Complement, suggest an active immunological response is part of the disease process. Similar pathways were also enhanced to varying extents in other non-myocyte cells and cardiomyocytes, in keeping with a broadly pro-inflammatory milieu (Fig. 1G). These findings highlight inflammation as a contributor to progressive remodeling from early stages, with chronic focal immune cell activation becoming prominent in later-stage HCM.

Similar RNA signature across HCM mouse models

To understand the temporal progression of HCM at the macroscopic and cellular levels, we employed the *Actc1*$^{\mathrm{E99K}}$ HCM mouse model, which not only recapitulates specific features of patients with the corresponding mutation (predominantly apical fibrosis and hypertrophy) (*36*) but also covers a spectrum of clinically relevant cardiac phenotypes with mild left ventricular hypertrophy (LVH), risk of sudden death and a marked tendency to adverse cardiac remodeling leading to heart failure. To ensure that our findings in this model were representative, we analyzed RNA profiles from four established HCM mouse models using GSEA and PROGENy on bulk RNA-seq data. The *Actc1*$^{\mathrm{E99K}}$ model is a transgenic line backcrossed onto a C57BL/6 background (*37*), demonstrating progressive hypertrophy and fibrosis from one to over twelve months, with systolic function initially preserved at 5 weeks but later reduced. The cardiac myosin heavy chain α - R403Q/+ and R719W/+, (*α-Mhc* $^{\mathrm{R403Q/+}}$ and *α-Mhc* $^{\mathrm{R719W/+}}$) models were generated on a 129/SyJ background by homologous recombination and, by 35 weeks, show cardiac hypertrophy, mild fibrosis, and diastolic dysfunction with preserved systolic function, mimicking typical HCM pathology (*15, 38, 39*). The cardiac troponin T2 – R92W (*TnT* $^{\mathrm{R92W}}$) model, a transgenic line backcrossed to C57BL/6 background for six generations, exhibits a threefold increase in fibrosis by 24 weeks with preserved systolic function and no hypertrophy (*40, 41*).

GSEA revealed common downregulation of oxidative phosphorylation and upregulation of epithelial-mesenchymal transition hallmark gene sets across all models, with largely shared immune-related pathways such as TNF-α Signaling By NFκB, IFN-α and γ responses, Inflammatory responses, interleukin-6 (IL-6)-Janus kinase (JAK)-signal transducer and activator of transcription 3 (STAT3) and interleukin-2 (IL-2)- STAT5 Signaling, Complement, and Allograft Rejection (Fig. 2A). PROGENy analysis, a computational tool used to infer pathway activity (*34*), confirmed consistent upregulated activity of Transforming Growth Factor-beta (TGF-β), Epidermal

Growth Factor Receptor (EGFR), Phosphoinositide 3-Kinases (PI3K), Hypoxia, and JAK-STAT pathways, showing consistency across the models (Fig. 2, B and C).

Relationship between immune cells and progressive remodeling in *Actc1*$^{\mathrm{E99K}}$ hearts

Post-weaning *Actc1*$^{\mathrm{E99K}}$ mice (4 to 6 weeks) exhibited apical hypertrophy and fibrosis with no changes in left ventricle posterior wall thickness (LVPW:d), ejection fraction (EF%), and left atrial (LA) size (Fig. 3, A to D and fig. S1, A to I), which represents an early stage of HCM with preserved systolic function. Entering adolescence and early maturation (8 to 24 weeks), *Actc1*$^{\mathrm{E99K}}$ mice underwent adverse tissue remodeling, not only in the apex with enhanced hypertrophy and fibrosis, but extended to other parts of the heart, including LV wall thickening, LV fibrosis, reduced EF%, and dilated LA (Fig. 3, A to D and fig. S1, A to I). This reflects the progression towards the advanced stage of HCM with reduced EF%. A marginal but significant accumulation of CD45^{+} immune cells emerged from approximately 10 weeks and continued to increase to three-fold at 24 weeks in *Actc1*$^{\mathrm{E99K}}$ hearts (Fig. 3E). Mature *Actc1*$^{\mathrm{E99K}}$ mice (24 to 36 weeks) showed slower exacerbation in cardiac hypertrophy, fibrosis, EF%, and LA dilatation (Fig. 3, A to D and fig. S1, A to I). However, immune cells almost doubled in *Actc1*$^{\mathrm{E99K}}$ hearts during the same period (Fig. 3E). No such changes were noticed in non-transgenic littermate wildtype animals (*Actc1*$^{\mathrm{NTG}}$). From middle age onwards (> 40 weeks), *Actc1*$^{\mathrm{E99K}}$ mice entered an accelerating phase of substantial hypertrophy and fibrosis in all regions with further reduced EF% and marked LA dilatation (Fig. 3, A to D and fig. S1, A to I), which represents the end stage of HCM. At a year, as in patients, *Actc1*$^{\mathrm{E99K}}$ hearts were characterized by prominent immune cell infiltration when compared to their age-matched controls (Fig. 3E). These data described a dynamic relationship between immune cell accumulation and progressive adverse remodeling in *Actc1*$^{\mathrm{E99K}}$ hearts.

Dynamic and active immune profile in *Actc1*$^{\mathrm{E99K}}$ hearts

Longitudinal immunophenotyping of *Actc1*$^{\mathrm{E99K}}$ hearts revealed dynamic changes of individual immune cell populations. The overall myeloid cells increased gradually for the first 36 weeks, followed by a sharp increase thereafter, whereas lymphocytes maintained a consistent 3 to 4-fold increase (Fig. 4, A to D). Nevertheless, cells from the myeloid lineage exhibited distinct temporal changes. For example, CD11b$^+$ F4/80$^+$ macrophages were the major early responsive immune cells (Fig. 4, E and F). Monocytes were the most representative of myeloid cells (Fig. 4G). Dendritic cells (DCs), the classic antigen presenting cells (APCs), increased concomitantly with T cells, which correlated closely with the progression of adverse remodeling in *Actc1*$^{\mathrm{E99K}}$ hearts (Fig. 4H). Increased numbers of neutrophils and eosinophils (Fig. 4, I to K) were found in the late stage, likely marking the loss of tissue homeostasis. Unlike others, natural killer cells peaked during maturation, followed by a decline afterwards (Fig. 4L). The flow cytometric gating strategy for cardiac immunophenotyping is exemplified in fig. S2A. No changes of CD45$^+$ immune cells were observed in spleen, blood, bone marrow, lung, or skeletal muscle from *Actc1*$^{\mathrm{E99K}}$ mice (fig. S2B). Cell DIVE imaging illustrated the presence of clustered CD45$^+$ immune cells in the fibrotic area of the *Actc1*$^{\mathrm{E99K}}$ heart (Fig. 4M).

We also observed the upregulation of cytokines and chemokines in *Actc1*$^{\mathrm{E99K}}$ hearts at mRNA and protein levels (fig. S3, A and B). These include CCL2, CCL3, CXCL1, CXCL2, and CXCL10, which support the observation of infiltrative immune cells. In addition, several classic pro-inflammatory and pro-fibrotic factors, including IL-1β, IL-6, IL-33, and TGF-β1, were augmented (fig. S3, A and B). No changes were detected for IL-2, IL-4, IL-5, and IL-10 at protein level (fig. S3B). These data provided evidence of an active and progressive inflammatory response in *Actc1*$^{\mathrm{E99K}}$ hearts.

Worsen cardiac fibrosis and dysfunction in *Actc1*$^{\mathrm{E99K}}$ hearts without lymphocytes

Lymphocyte activation has been implicated in mouse models of autoimmune myocarditis (*28*), heart failure (*29*), and dilated cardiomyopathy (*42, 43*). To investigate the role of lymphocytes in HCM, we generated an HCM mouse model with lymphocyte deficiency (*Actc1*$^{\mathrm{E99K}}$ *Rag-1*$^{\mathrm{KO}}$). We employed late gadolinium enhancement (LGE)-cardiac magnetic resonance (CMR) imaging to monitor the development of LV fibrosis and wall thickness in live mice. Diffuse fibrosis in LV mid-wall was documented in *Actc1*$^{\mathrm{E99K}}$ mice at 24 weeks, which was further enhanced in age matched *Actc1*^{E99K} *Rag-1*^{KO} mice (Fig. 5A). Apical fibrosis was detected using Sirius Red or Masson Trichrome staining in a long axis setting. Fibrosis analysis of individual regions confirmed that *Actc1*^{E99K} *Rag-1*^{KO} mice exacerbated LV, but not apical or atrial fibrosis (Fig. 5, B to E). This was accompanied by further thickening of the LV mid-wall, reduced EF% and elevated end diastolic pressure but not overall cardiac hypertrophy (Fig. 5, F to I). This exaggerated remodeling presented as early as 10 weeks (fig. S4, A to D).

More myeloid cells were found in *Rag-1*^{KO} mice when compared to *Actc1*^{NTG}, presumably as a compensatory mechanism for the loss of adaptive immunity (fig. S4E). Of note, this myeloid cell accumulation alone did not result in excessive fibrosis (Fig. 5A) nor systolic dysfunction (fig. S4A) in *Rag-1*^{KO} mice. In fact, the myeloid lineage further expanded in *Actc1*^{E99K} *Rag-1*^{KO} mice when compared to *Rag-1*^{KO} mice (fig. S4E). In addition, bulk RNA-seq analysis suggested further upregulated inflammatory and downregulated metabolic pathways in *Actc1*^{E99K} *Rag-1*^{KO} hearts when compared to *Actc1*^{E99K} hearts (fig. S4F). These data suggest that the activation of accumulated myeloid cells in response to mutant cardiomyocytes may explain excessive LV fibrosis and exacerbated systolic dysfunction found in *Actc1*^{E99K} *Rag-1*^{KO} hearts. Importantly, this experiment implicates one or more member(s) of the lymphoid lineage in protecting against cardiac fibrosis and dysfunction in HCM hearts.

Enrichment of functionally altered Foxp3^{+} Tregs in HCM hearts

Tregs are a well characterized lymphocyte subset with potent immunosuppressive function (*30*). To date, the role of Tregs in HCM has not been investigated. A higher frequency of Tregs in CD4^{+} T cells was observed in the heart using flow cytometry, but not the lung or skeletal muscle from *Actc1*^{E99K} mice, suggesting that Tregs only accumulated at the site of inflammation (Fig. 6A). This accumulation was progressive in the heart, at least from 24 weeks onwards (Fig. 6B). Further analysis found that Tregs from approximately 40 weeks *Actc1*^{E99K} hearts exhibited higher expression of CD44, CD25, inducible T-cell co-stimulator (ICOS), and programme cell death protein 1 (PD-1), suggesting that they were recruited and activated. Although GATA-binding factor 3 (GATA-3), a known transcription factor for Treg tissue-retention (*44*), was elevated, no additional increase of immunosuppressive cytokines (TGF-β1 and IL-10) were found (Fig. 6C and fig. S5, A to K). No pro-inflammatory markers were noted (fig. S5, L, M, and P).

Next, we investigated the gene profile of Tregs from *Actc1*^{E99K} and *Actc1*^{NTG} hearts using single cell RNA-seq. Cardiac Tregs from 45 weeks *Actc1*^{NTG} mice showed a classic Treg gene signature, including *Foxp3*, *Ikzf2*, *Gata3*, *Ctla4*, *Tgfb1*, *Il10ra*, and *Ebi3* (Fig. 6D). In comparison to conventional CD4^{+} T cells (Tconv), cardiac Tregs from *Actc1*^{NTG} mice were in an active state with higher expression of transcriptional factors related to immunosuppression (for example, *Nrp1*, *Nr4a1*, and *Gata-3*), elevated activation markers (for example, *Icos*, *Cd69*, *Klrg1*, *Ifnar1*, and *Il1rl1*), enhanced metabolic manipulation markers (for example, *Il2ra*, and *Entpd1*), increased inhibitory cytokines (for example, *Tgfb1*, *Il10ra*, and *Ebi3*), boosted cytolysis (for example, *Gzmb*), and uplifted immune checkpoints (for example, *Ctla4*, *Tigit*, *Havcr2*, and *Tnfrsf18*). Compared to their counterpart from *Actc1*^{NTG} hearts, cardiac Tregs from *Actc1*^{E99K} exhibited reduced expression of immunosuppression associated transcriptional factors (for example, *Nrp1*, *Nr4a1*, and *Gata-3*), decreased activation markers (for example, *Cd69*, *Klrg1*, *Ifnar1*, and *Il1rl1*), diminished metabolic manipulation (for example, *Il2ra*), reduced inhibitory cytokines (for example, *Tgfb1*, *Il10ra*, and *Ebi3*), and less cytolysis (for example, *Gzmb*), but upregulated immune checkpoints, including *Ctla4*, *Tigit*, *Havcr2*, and *Lag3*.

A similar pattern was observed in cardiac Tregs from patients with end-stage HCM when compared to non-failing controls using the snRNA data from the public domain. Again, control Tregs showed basal activity of Treg function including *FOXP3*, *IKZF2*, *GATA-3, ICOS*, *IL2RA*, *ENTPD1*, *TGFB1*, *IL10RA*, *CTLA4*, *TIGIT*, and *PDCD1* (Fig. 6E). HCM Tregs exhibited reduced expression of genes in metabolic manipulation and inhibitory cytokines, but upregulated expression of those in immune checkpoints. These data suggested that cardiac Tregs may alter mechanism(s) for action during chronic inflammation in HCM mouse and human hearts.

Ameliorated cardiac fibrosis and dysfunction following adoptive transfer of Tregs

We next investigated whether Treg enrichment could be beneficial to HCM hearts. In brief, live splenic CD4$^+$ Foxp3$^+$ Tregs sorted from wildtype donors were adoptively transferred into either *Actc1*$^{\mathrm{E99K}}$ *Rag-1*$^{\mathrm{KO}}$ or *Rag-1*$^{\mathrm{KO}}$ recipient mice twice in 8 weeks. A significant reduction of EF% was already present in *Actc1*$^{\mathrm{E99K}}$ *Rag-1*$^{\mathrm{KO}}$ mice when compared to *Rag-1*$^{\mathrm{KO}}$ mice at 24 weeks of age, followed by a gradual decline within the study period (Fig. 7A). No such change was noticed in *Rag-1*$^{\mathrm{KO}}$ mice. EF% was significantly improved in those *Actc1*$^{\mathrm{E99K}}$ *Rag-1*$^{\mathrm{KO}}$ mice with Tregs after 3 weeks when compared to those with PBS vehicle and continued to improve up to 8 weeks when compared to pre-transfer echo baseline in the same group (Fig. 7A). LV end systolic volume (LVESV) reciprocated the trend of EF% in *Actc1*$^{\mathrm{E99K}}$ *Rag-1*$^{\mathrm{KO}}$ mice, which was largely rescued with the addition of Tregs (Fig. 7B). No such changes were noticeable in LV wall thickness or LA size (Fig. 7, C and D). Further analysis indicated that this approach diminished apical and LV fibrosis by at least 50% without altering overall cardiac hypertrophy (Fig. 7, E to G and fig. S6A). These data demonstrate that Tregs can ameliorate cardiac fibrosis and improve contractile function but not ventricular hypertrophy or LA dilatation in *Actc1*$^{\mathrm{E99K}}$ *Rag-1*$^{\mathrm{KO}}$ mice, probably in a lymphocyte-independent manner.

We next investigated the effect of Tregs adoptive transfer in the presence of lymphocytes in *Actc1*$^{\mathrm{E99K}}$ mice. The result indicated that Treg enrichment could indeed prevent further deterioration in contractile function (Fig. 7, H and I) with no impact on LV wall thickness nor LA size (Fig. 7, J and K) and reduce apical and LV fibrosis (Fig. 7, L to N) without any impact on cardiac hypertrophy (fig. S6D). These data suggests that Treg enrichment may be a therapeutic strategy for patients with HCM.

Suppressed macrophage activation and limited fibrosis by IL-2 therapies

To examine the therapeutic potential of Treg therapy, IL-2/IL-2 mAb complex (IL-2/c)-induced Treg expansion in vivo was tested in *Actc1*$^{\mathrm{E99K}}$ mice. Low dose IL-2 therapy has been reported in clinical trials to treat autoimmune and rheumatic diseases through its ability to expand Treg numbers and boost their activity to suppress unwanted inflammation (*45*). We chose the low dose IL-2/c protocol to specifically and maximally expand immunosuppressive Tregs in vivo (*46*).

Preliminary data indicated that low dose, high frequency IL-2/c sufficiently boosted Treg numbers in the heart, the spleen, and mediastinal lymph nodes (fig. S7A). This effect was dose-dependent (from 0.375, 0.75, to 1.5 μg of recombinant mouse IL-2/c, rmIL-2/c), which gave rise to 30%, 50%, and 70% of Tregs in cardiac CD4$^+$ T cells, respectively (fig. S7, B to D). However, even the very low dose of rmIL-2/c (0.375 μg) resulted in elevated lung and spleen weight (but not heart weight) with labored breathing in *Actc1*$^{\mathrm{E99K}}$ mice but not *Actc1*$^{\mathrm{NTG}}$ mice within three weeks of treatment (fig. S7, E to G). This suggests the presence of vascular leak syndrome (VLS), which is known to be associated with high dose IL-2 treatment (15 μg or 250,000 IU of IL-2) (*46*). Reducing frequency (twice per week for 8 weeks) with low dose IL-2/c (1.5 μg) treatment delayed the onset of VLS but could not eliminate it (fig. S7, A and F).

Nevertheless, within the study period of the treatment, either very low dose (0.375 μg of rmIL-2/c) with high frequency (5 times first week followed by twice a week for 3 weeks) or low dose (1.5 μg of rmIL-2/c) with low frequency (two consecutive injections every two weeks for 8 weeks) IL-2/c treatment significantly protected *Actc1*$^{\mathrm{E99K}}$ hearts from further deterioration in systolic dysfunction but not LA size (Fig. 8, A to D) and ventricular fibrosis (Fig. 8, E to G).

When we investigated the potential mechanism underpinning these effects, we found that both regimens markedly dampened the infiltration of macrophages, and to a lesser degree dendritic cells in *Actc1*$^{\mathrm{E99K}}$ hearts (Fig. 8, H and I). In addition, major histocompatibility complex II+ (MHCII$^+$) macrophages were significantly reduced, whereas MHCII$^+$ DCs were less affected by either treatment (Fig. 8, J and K). Toll-like receptor-2 (TLR-2$^+$) macrophages were significantly diminished following either treatment (Fig. 8, L and M), suggesting Tregs negatively regulate the recruitment and activation of inflammatory cells with a preferential effect on macrophages.

Further flow cytometric analysis revealed that even very low dose IL-2/c enhanced Treg tissue retention marker GATA-3 and immunosuppressive molecule TGF-β1 (Fig. 8, N to P), but not interleukin-10 (IL-10), TNF-α, or IFN-γ expression (fig. S7H) in cardiac $CD4^+$ $Foxp3^+$ Tregs. Thus, Tregs appear to play a role in modulating cardiac fibrosis and systolic dysfunction by suppressing unwanted chronic infiltration and inflammation in *Actc1*^{E99K} hearts.

DISCUSSION

HCM-causing sarcomere gene mutations alter contractility, leading to metabolic and energetic perturbations in cardiomyocytes. These causative variants occur both in thick filament genes (for example, *MYH7* and *MYBPC3*) and thin filament genes (for example, *TPM1*, *TNNT2*, *TNNI*, and *ACTC1*) with shared features at myofilament level. However, little is known about subsequent events leading to pathogenic tissue remodeling including fibrosis. GSEA comparing RNA signatures from mid-stage myectomy samples and end-stage failing HCM hearts revealed a progressive fibrotic and inflammatory responses following contractile and metabolic alterations in mutant cardiomyocytes. Identifying non-myocyte cell populations that drive fibrosis and inflammation is crucial for developing disease-modifying therapies. As human samples capture only a snapshot of the disease, the well-established *Actc1*^{E99K} HCM mouse model (*37*) was employed to investigate progressive adverse remodeling and evaluate therapeutic interventions. This transgenic model exhibited hypertrophy comparable to other HCM mouse models, along with robust remodeling and systolic dysfunction (*15, 41*). Although a wildtype overexpression control for the E99K mutant was unavailable, previous studies confirmed that paired expression of wildtype thin filament transgenes produces no discernible phenotype (*47-49*). Our findings demonstrate that the RNA signature was conserved across four HCM mouse models and that immune cells contributed to HCM pathologic remodeling in both humans and mice. Most importantly, we identify an essential role for Tregs in mitigating cardiac fibrosis and systolic dysfunction by suppressing the recruitment and activation of proinflammatory immune cells.

Unlike myocarditis, where inflammatory activation is well documented, immune cell infiltration and chronic inflammation remain poorly defined in HCM. Transcriptomic studies confirmed the presence of immune cells in the heart but offer limited insights into their role(s) in disease progression (*32, 33*). To systematically investigate immune involvement in HCM pathogenesis, we employed a multifaceted approach: cellular and molecular analysis of post-mortem or explant tissue from patients with HCM using imaging and RNA seq, longitudinal phenotyping of progressive cardiac remodeling and immune responses in a HCM mouse model, and immunological manipulation to assess causal effects on adverse remodeling and cardiac function. Our data revealed moderate immune cell infiltration, with a significantly upregulated inflammatory gene profile shared across multiple cardiac cell types in both human and mouse HCM hearts. This infiltration might be actively coordinated by endothelial cells through increased barrier permeability and adhesion molecule expression. Additionally, fibroblasts and adipocytes might also contribute by secreting chemokines and cytokines that recruit and activate immune cells. Inflammatory responses were elevated across most cardiac cell types, including cardiomyocytes and non-cardiomyocytes, indicating the establishment of a persistent inflammatory milieu. This unresolved chronic inflammation likely serves as a key driver of the progressive adverse remodeling in HCM.

We found further deterioration in cardiac fibrosis and systolic dysfunction in *Actc1*$^{\mathrm{E99K}}$ *Rag-1*$^{\mathrm{KO}}$ mice. This is opposite to the protective effect provided by either antibody-mediated CD4^{+} T cell depletion or using the *Rag-1*$^{\mathrm{KO}}$ mice in an autoimmune myocarditis model induced by myosin peptide or mimics (*50, 51*). This observation suggests some lymphocytes may counteract the pathology. Myeloid cells, on the other hand, may contribute to the pathogenesis, a theme borne out in observational clinical studies linking higher blood monocyte count with shortened survival in HCM (*52*). Although dynamic changes of individual innate immune cell subsets are of importance and warrant further investigation, we chose to focus on identifying the lymphocyte subset(s) that could ameliorate cardiac fibrosis and dysfunction in this study as this has direct clinical applicability.

Among those possible candidates, Tregs are well-documented T cells with known capacity to suppress unwanted immune response through at least four different mechanisms, including suppression through anti-inflammatory cytokines, immune checkpoint molecules, cytolysis, and metabolic manipulation. However, dysfunctional Tregs can be pathogenic when they behave like Th1/Th17 helper T cells to amplify inflammatory responses (*53*). Tregs further denominate into tissue-specific Tregs, with dedicated adaption to their local environment (for example, the lung, visceral adipose tissue, skin, intestine, and skeletal muscle) for priming survival or function (*54*). They have been shown to modulate muscle injury and inflammation in the *Mdx* mouse model of Duchenne Muscular Dystrophy, by suppressing IFN-γ response and activation of M1 macrophages (*55*). Treg in vivo expansion has been shown to ameliorate many cardiac diseases with a known inflammatory response, including myocardial infarction (*56, 57*), viral myocarditis (*58*), diabetic cardiomyopathy (*59*), angiotensin II-induced cardiac damage (*60*), hypertension (*61*) and ischemic heart failure (*53, 62*). Therefore, it is important to characterize cardiac Tregs in detail and establish their potential to limit fibrosis in HCM.

Tregs were confirmed in HCM human and mouse hearts using snRNA seq, flow cytometry, and imaging. *Actc1*$^{\text{E99K}}$ hearts exhibited a sustained increase of Tregs, similar in magnitude compared to myocardial infarction (MI) or ischemia/reperfusion (I/R) injury models with a transient rise (*56*), where Tregs suppress acute inflammation. Mechanisms governing Treg-mediated suppression may differ in acute versus chronic settings. In acute injury, interleukin-33 (IL-33)/interleukin 1 receptor-like 1 (IL1RL1 or ST2) signaling may drive transient Treg expansion, but it fails to rescue cardiac dysfunction or reduce scarring (*56*). In HCM, a chronic setting, Tregs showed reduced ST2 expression, suggesting alternative signals may regulate their accumulation and immunosuppressive function.

In non-HCM hearts, both mouse and human Tregs seem to be mature thymus-derived cells (for example, *Ikzf2*, *Tigit*, *Il2ra*, *Ctla4*, and *Icos*) with an active format (for example, *Gata3*, *Tgfb1*, *Tigit*, *Il2ra*, *Ctla4*, and *Icos*), suggesting that Treg activities are required for maintaining cardiac homeostasis. Upon chronic inflammation in

HCM hearts, it seemed that they might have switched their suppressive action from inhibitory cytokines (for example, *Tgfb1, Il10ra,* and *Ebi*) to immune checkpoint molecules (for example, *Ctla4, Tigit*, *Lag3* and *Pdcd-1*). This change may reflect a need to establish cell-cell contacts for Tregs to control inflammatory cells that are growing in numbers and activation status in HCM hearts. It is plausible that the efficiency of Treg-mediated immunosuppression could be reduced due to the switch to physical contact rather than humoral control, even though their numbers and activities are upregulated in HCM. It also remains possible that Tregs may directly or indirectly modulate other cardiac cell types including cardiomyocytes and fibroblasts. Spatial RNA-seq analysis on pathological foci may offer further understanding of the location and mechanism(s) of this Treg-mediated immunosuppression.

Our study has several limitations. We acknowledge the limitations of animal models in studying HCM, as they may not fully reflect human clinical complexity. Firstly, there are species differences in cardiac pathophysiology. For instance, the murine heart rate (around 600 beat per minute) is approximately 10-fold higher than in humans, which fundamentally alters cardiac metabolism, calcium handling, response to stress, and the rate of disease progression. Although progressive phases of the disease can be recapitulated using HCM animal models, the penetration of pathogenic variants, magnitude of responses, and duration of disease progression may differ in patients with HCM. Secondly, there are considerable genetic and environmental variability. The population of patients with HCM is heterogenous, carrying sarcomeric positive or negative mutations or with unknown causes. On the other hand, four HCM mouse models used in the study were sarcomeric positive models and most of data was obtained from the *Actc1*$^{\mathrm{E99K}}$ transgenic model on a C57BL/6 background when compared to non-transgenic littermate wildtypes. In addition, delineating the roles of limited cardiac Tregs and determining the optimal dosage and timing for immunomodulatory intervention remain key challenges and warrant further investigation. Although adoptive transfer of Tregs in *Actc1*$^{\mathrm{E99K}}$ *Rag-1*$^{\mathrm{KO}}$ mice improved cardiac fibrosis and systolic dysfunction, we acknowledge that we have not shown the timing of treatment for the reversal of fibrosis in *Actc1*$^{\mathrm{E99K}}$ mice, and future work should address this.

Our work demonstrates that augmenting Tregs protects the HCM heart from further deterioration caused by cardiac fibrosis and dysfunction, likely through their immunosuppressive properties. This intervention prevents further adverse remodeling, and may potentially reverse it, offering therapeutic potential for patients with HCM entering the ‘burned out stage’ of the disease (*20, 63*). Additionally, Treg-based therapy could serve as adjunctive treatments alongside disease-modifying therapies aiming to correct the underlying cardiomyocyte defects. Given the promising result of Treg therapies in clinical trials for other diseases, these strategies may be ready for clinical evaluation as a viable therapeutic option for HCM.

MATERIALS AND METHODS

Study Design

This study aimed to characterize immune infiltration and inflammation in HCM patient hearts using imaging and RNA-seq, to conduct a longitudinal study on cardiac adverse remodeling and immune changes using an HCM mouse model (*Actc1*$^{\mathrm{E99K}}$), and to assess the therapeutic potential of Treg enrichment in modulating cardiac fibrosis in HCM. Formalin fixed paraffin embedded (FFPE) human post-mortem or explanted heart tissues were obtained with patient consent from Cambridge University Hospitals, Royal Papworth Hospital, and Oxford University Hospitals tissue banks with full ethical approval (IRAS: 162057; PI: Prof. E. Soilleux). Samples included healthy controls (n=10), HCM (n=16), myocarditis (n=7), and heart failure (n=6) confirmed by two pathologists. Cases of lymphocytic myocarditis or heart failure were included only when no history of primary cardiomyopathy was found. SnRNA-seq data were analyzed using public datasets from myectomy tissue (HCM: n=10, controls: n=2) (*33*) and LV samples (failing HCM: n=15, non-failing: n=16) (*32*).

All littermate wildtype, heterozygous, and homozygous mice were housed and bred under specific pathogen-free (SPF) conditions. Maintenance and procedures were reviewed by the local Animal Welfare and Ethical Review Body (AWERB) and conducted under project licenses (30/2977 / P37BA1809 / PP2089735) authorized by the

UK Home Office. The *Actc1*^{E99K} model, originally generated on a C57BL10xCBA/Ca background, was backcrossed onto C57BL/6 (mixed 6N and 6J) background for over ten generations. Only heterozygous *Actc1*^{E99K} and *Actc1*^{NTG} littermates were used in the study (no homozygous E99K). *Rag*-1^{KO} mice (gift from Prof. Fiona Powrie) were crossed to create the *Actc1*^{E99K} *Rag-1*^{KO} model. The *Foxp3*$^{tm3(DTR/GFP)Ayr}$/J knock-in mice (Jackson Laboratory) were used to generate the *Actc1*^{E99K} *Foxp3*$^{DTR/GFP}$ model. Following the Animals in Research: Reporting In Vivo Experiments (ARRIVE) guidelines, we introduced a randomizing, blinding, and blocking scheme to perform cardiac phenotyping using mouse ID without indicating the genotype. Data was analyzed by another colleague unfamiliar with the experimental design in case of overt phenotypes. This included longitudinal echocardiography (n≥5 for each time point), haemodynamic studies (n≥4 for each time point), and LGE-MRI for LV interstitial fibrosis (n=5-6 for each time point). Sample sizes were estimated based on our previous experience with each technique. Outliers are shown in the raw data. Any data that was excluded from this study is described in the relevant sections. Under the guidance of National Centre for the 3Rs (NC3R), males and females were recruited, and multiplexing approach was adopted to reduce the use of animals.

Statistical analysis

Statistical analysis was performed using GraphPad Prism 9.5 or higher. One-way ANOVA was used for normally distributed data, including cardiac phenotyping, Treg percentages across tissues, and Treg enrichment studies. Nonparametric Kruskal-Wallis and Mann-Whitney tests were applied for non-normally distributed data across multiple or two groups, respectively. two-way ANOVA mixed-effects analysis was used for longitudinal cardiac/immune phenotyping, Treg time-course, and enrichment experiments. Multiple comparisons were corrected using the Benjamini-Krieger-Yekutieli or Šidák method. Data are presented as mean ± SEM. Statistical significance was set at $p < 0.05$ for two groups and adjusted $p < 0.05$ for three or more groups. Figures use star markers for *p*-values (* < 0.05, ** < 0.01, *** < 0.001, **** < 0.0001, ns ≥ 0.05) and delta markers for additional comparisons (Δ < 0.05, ΔΔ < 0.01, ΔΔΔ < 0.001).

List of Supplementary Materials

Materials & Methods

Figures S1 to S7

Tables S1 to S7

Data file S1 to S4

References (64-88)

MDAR Reproducibility checklist

References

1. H. Watkins, H. Ashrafian, C. Redwood, Inherited cardiomyopathies. *N Engl J Med* **364**, 1643-1656 (2011).
2. R. Yotti, C. E. Seidman, J. G. Seidman, Advances in the Genetic Basis and Pathogenesis of Sarcomere Cardiomyopathies. *Annu Rev Genomics Hum Genet* **20**, 129-153 (2019).
3. B. J. Maron, E. J. Rowin, M. S. Maron, Evolution of risk stratification and sudden death prevention in hypertrophic cardiomyopathy: Twenty years with the implantable cardioverter-defibrillator. *Heart Rhythm* **18**, 1012-1023 (2021).
4. C. Y. Ho, S. M. Day, E. A. Ashley, M. Michels, A. C. Pereira, D. Jacoby, A. L. Cirino, J. C. Fox, N. K. Lakdawala, J. S. Ware, C. A. Caleshu, A. S. Helms, S. D. Colan, F. Girolami, F. Cecchi, C. E. Seidman, G. Sajeev, J. Signorovitch, E. M. Green, I. Olivotto, Genotype and Lifetime Burden of Disease in Hypertrophic Cardiomyopathy: Insights from the Sarcomeric Human Cardiomyopathy Registry (SHaRe). *Circulation* **138**, 1387-1398 (2018).
5. J. A. Jarcho, W. McKenna, J. A. Pare, S. D. Solomon, R. F. Holcombe, S. Dickie, T. Levi, H. Donis-Keller, J. G. Seidman, C. E. Seidman, Mapping a gene for familial hypertrophic cardiomyopathy to chromosome 14q1. *N Engl J Med* **321**, 1372-1378 (1989).
6. A. A. Geisterfer-Lowrance, S. Kass, G. Tanigawa, H. P. Vosberg, W. McKenna, C. E. Seidman, J. G. Seidman, A molecular basis for familial hypertrophic cardiomyopathy: a beta cardiac myosin heavy chain gene missense mutation. *Cell* **62**, 999-1006 (1990).
7. H. Watkins, W. J. McKenna, L. Thierfelder, H. J. Suk, R. Anan, A. O'Donoghue, P. Spirito, A. Matsumori, C. S. Moravec, J. G. Seidman, et al., Mutations in the genes for cardiac troponin T and alpha-tropomyosin in hypertrophic cardiomyopathy. *N Engl J Med* **332**, 1058-1064 (1995).
8. R. Walsh, K. L. Thomson, J. S. Ware, B. H. Funke, J. Woodley, K. J. McGuire, F. Mazzarotto, E. Blair, A. Seller, J. C. Taylor, E. V. Minikel, C. Exome Aggregation, D. G. MacArthur, M. Farrall, S. A. Cook, H. Watkins, Reassessment of Mendelian gene pathogenicity using 7,855 cardiomyopathy cases and 60,706 reference samples. *Genet Med* **19**, 192-203 (2017).
9. A. A. Alfares, M. A. Kelly, G. McDermott, B. H. Funke, M. S. Lebo, S. B. Baxter, J. Shen, H. M. McLaughlin, E. H. Clark, L. J. Babb, S. W. Cox, S. R. DePalma, C. Y. Ho, J. G. Seidman, C. E. Seidman, H. L. Rehm, Results of clinical genetic testing of 2,912 probands with hypertrophic cardiomyopathy: expanded panels offer limited additional sensitivity. *Genet Med* **17**, 880-888 (2015).
10. J. G. Crilley, E. A. Boehm, E. Blair, B. Rajagopalan, A. M. Blamire, P. Styles, W. J. McKenna, I. Ostman-Smith, K. Clarke, H. Watkins, Hypertrophic cardiomyopathy due to sarcomeric gene mutations

is characterized by impaired energy metabolism irrespective of the degree of hypertrophy. *J Am Coll Cardiol* **41**, 1776-1782 (2003).

11. S. Vakrou, M. R. Abraham, Hypertrophic cardiomyopathy: a heart in need of an energy bar? *Frontiers in Physiology* **5**, (2014).
12. J. van der Velden, C. G. Tocchetti, G. Varricchi, A. Bianco, V. Sequeira, D. Hilfiker-Kleiner, N. Hamdani, A. F. Leite-Moreira, M. Mayr, I. Falcao-Pires, T. Thum, D. K. Dawson, J. L. Balligand, S. Heymans, Metabolic changes in hypertrophic cardiomyopathies: scientific update from the Working Group of Myocardial Function of the European Society of Cardiology. *Cardiovasc Res* **114**, 1273-1280 (2018).
13. A. M. Varnava, P. M. Elliott, S. Sharma, W. J. McKenna, M. J. Davies, Hypertrophic cardiomyopathy: the interrelation of disarray, fibrosis, and small vessel disease. *Heart* **84**, 476-482 (2000).
14. C. Y. Ho, B. Lopez, O. R. Coelho-Filho, N. K. Lakdawala, A. L. Cirino, P. Jarolim, R. Kwong, A. Gonzalez, S. D. Colan, J. G. Seidman, J. Diez, C. E. Seidman, Myocardial fibrosis as an early manifestation of hypertrophic cardiomyopathy. *N Engl J Med* **363**, 552-563 (2010).
15. P. Teekakirikul, S. Eminaga, O. Toka, R. Alcalai, L. Wang, H. Wakimoto, M. Nayor, T. Konno, J. M. Gorham, C. M. Wolf, J. B. Kim, J. P. Schmitt, J. D. Molkentin, R. A. Norris, A. M. Tager, S. R. Hoffman, R. R. Markwald, C. E. Seidman, J. G. Seidman, Cardiac fibrosis in mice with hypertrophic cardiomyopathy is mediated by non-myocyte proliferation and requires Tgf-beta. *J Clin Invest* **120**, 3520-3529 (2010).
16. A. Axelsson Raja, H. Farhad, A. M. Valente, J. P. Couce, J. L. Jefferies, H. Bundgaard, K. Zahka, H. Lever, A. M. Murphy, E. Ashley, S. M. Day, M. V. Sherrid, L. Shi, D. A. Bluemke, C. E. Canter, S. D. Colan, C. Y. Ho, Prevalence and Progression of Late Gadolinium Enhancement in Children and Adolescents With Hypertrophic Cardiomyopathy. *Circulation* **138**, 782-792 (2018).
17. B. Raman, R. Ariga, M. Spartera, S. Sivalokanathan, K. Chan, S. Dass, S. E. Petersen, M. J. Daniels, J. Francis, R. Smillie, A. J. Lewandowski, E. O. Ohuma, C. Rodgers, C. M. Kramer, M. Mahmod, H. Watkins, S. Neubauer, Progression of myocardial fibrosis in hypertrophic cardiomyopathy: mechanisms and clinical implications. *Eur Heart J Cardiovasc Imaging* **20**, 157-167 (2019).
18. M. Habib, A. Adler, K. Fardfini, S. Hoss, K. Hanneman, E. J. Rowin, M. S. Maron, B. J. Maron, H. Rakowski, R. H. Chan, Progression of Myocardial Fibrosis in Hypertrophic Cardiomyopathy: A Cardiac Magnetic Resonance Study. *JACC Cardiovasc Imaging* **14**, 947-958 (2021).
19. J. J. Green, J. S. Berger, C. M. Kramer, M. Salerno, Prognostic value of late gadolinium enhancement in clinical outcomes for hypertrophic cardiomyopathy. *JACC Cardiovasc Imaging* **5**, 370-377 (2012).
20. E. Biagini, F. Coccolo, M. Ferlito, E. Perugini, G. Rocchi, L. Bacchi-Reggiani, C. Lofiego, G. Boriani, D. Prandstraller, F. M. Picchio, A. Branzi, C. Rapezzi, Dilated-hypokinetic evolution of hypertrophic cardiomyopathy: prevalence, incidence, risk factors, and prognostic implications in pediatric and adult patients. *J Am Coll Cardiol* **46**, 1543-1550 (2005).
21. I. Olivotto, F. Cecchi, C. Poggesi, M. H. Yacoub, Patterns of disease progression in hypertrophic cardiomyopathy: an individualized approach to clinical staging. *Circ Heart Fail* **5**, 535-546 (2012).
22. S. M. Day, J. C. Tardiff, E. M. Ostap, Myosin modulators: emerging approaches for the treatment of cardiomyopathies and heart failure. *J Clin Invest* **132**, (2022).
23. D. Reichart, G. A. Newby, H. Wakimoto, M. Lun, J. M. Gorham, J. J. Curran, A. Raguram, D. M. DeLaughter, D. A. Conner, J. D. C. Marsiglia, S. Kohli, L. Chmatal, D. C. Page, N. Zabaleta, L. Vandenberghe, D. R. Liu, J. G. Seidman, C. Seidman, Efficient in vivo genome editing prevents hypertrophic cardiomyopathy in mice. *Nat Med* **29**, 412-421 (2023).
24. A. C. Chai, M. Cui, F. Chemello, H. Li, K. Chen, W. Tan, A. Atmanli, J. R. McAnally, Y. Zhang, L. Xu, N. Liu, R. Bassel-Duby, E. N. Olson, Base editing correction of hypertrophic cardiomyopathy in human cardiomyocytes and humanized mice. *Nat Med* **29**, 401-411 (2023).
25. S. Epelman, K. J. Lavine, A. E. Beaudin, D. K. Sojka, J. A. Carrero, B. Calderon, T. Brija, E. L. Gautier, S. Ivanov, A. T. Satpathy, J. D. Schilling, R. Schwendener, I. Sergin, B. Razani, E. C. Forsberg, W. M. Yokoyama, E. R. Unanue, M. Colonna, G. J. Randolph, D. L. Mann, Embryonic and adult-derived

resident cardiac macrophages are maintained through distinct mechanisms at steady state and during inflammation. *Immunity* **40**, 91-104 (2014).

26. M. Hulsmans, S. Clauss, L. Xiao, A. D. Aguirre, K. R. King, A. Hanley, W. J. Hucker, E. M. Wulfers, G. Seemann, G. Courties, Y. Iwamoto, Y. Sun, A. J. Savol, H. B. Sager, K. J. Lavine, G. A. Fishbein, D. E. Capen, N. Da Silva, L. Miquerol, H. Wakimoto, C. E. Seidman, J. G. Seidman, R. I. Sadreyev, K. Naxerova, R. N. Mitchell, D. Brown, P. Libby, R. Weissleder, F. K. Swirski, P. Kohl, C. Vinegoni, D. J. Milan, P. T. Ellinor, M. Nahrendorf, Macrophages Facilitate Electrical Conduction in the Heart. *Cell* **169**, 510-522 e520 (2017).
27. W. P. Lafuse, D. J. Wozniak, M. V. S. Rajaram, Role of Cardiac Macrophages on Cardiac Inflammation, Fibrosis and Tissue Repair. *Cells* **10**, (2020).
28. H. Lv, E. Havari, S. Pinto, R. V. Gottumukkala, L. Cornivelli, K. Raddassi, T. Matsui, A. Rosenzweig, R. T. Bronson, R. Smith, A. L. Fletcher, S. J. Turley, K. Wucherpfennig, B. Kyewski, M. A. Lipes, Impaired thymic tolerance to alpha-myosin directs autoimmunity to the heart in mice and humans. *J Clin Invest* **121**, 1561-1573 (2011).
29. T. Nevers, A. M. Salvador, A. Grodecki-Pena, A. Knapp, F. Velazquez, M. Aronovitz, N. K. Kapur, R. H. Karas, R. M. Blanton, P. Alcaide, Left Ventricular T-Cell Recruitment Contributes to the Pathogenesis of Heart Failure. *Circ Heart Fail* **8**, 776-787 (2015).
30. D. A. Vignali, L. W. Collison, C. J. Workman, How regulatory T cells work. *Nat Rev Immunol* **8**, 523-532 (2008).
31. J. Kuusisto, V. Karja, P. Sipola, I. Kholova, K. Peuhkurinen, P. Jaaskelainen, A. Naukkarinen, S. Yla-Herttuala, K. Punnonen, M. Laakso, Low-grade inflammation and the phenotypic expression of myocardial fibrosis in hypertrophic cardiomyopathy. *Heart* **98**, 1007-1013 (2012).
32. M. Chaffin, I. Papangeli, B. Simonson, A. D. Akkad, M. C. Hill, A. Arduini, S. J. Fleming, M. Melanson, S. Hayat, M. Kost-Alimova, O. Atwa, J. Ye, K. C. Bedi, Jr., M. Nahrendorf, V. K. Kaushik, C. M. Stegmann, K. B. Margulies, N. R. Tucker, P. T. Ellinor, Single-nucleus profiling of human dilated and hypertrophic cardiomyopathy. *Nature* **608**, 174-180 (2022).
33. X. Liu, K. Yin, L. Chen, W. Chen, W. Li, T. Zhang, Y. Sun, M. Yuan, H. Wang, Y. Song, S. Wang, S. Hu, Z. Zhou, Lineage-specific regulatory changes in hypertrophic cardiomyopathy unraveled by single-nucleus RNA-seq and spatial transcriptomics. *Cell Discov* **9**, 6 (2023).
34. M. Schubert, B. Klinger, M. Klunemann, A. Sieber, F. Uhlitz, S. Sauer, M. J. Garnett, N. Bluthgen, J. Saez-Rodriguez, Perturbation-response genes reveal signaling footprints in cancer gene expression. *Nat Commun* **9**, 20 (2018).
35. A. Liberzon, C. Birger, H. Thorvaldsdottir, M. Ghandi, J. P. Mesirov, P. Tamayo, The Molecular Signatures Database (MSigDB) hallmark gene set collection. *Cell Syst* **1**, 417-425 (2015).
36. L. Monserrat, M. Hermida-Prieto, X. Fernandez, I. Rodriguez, C. Dumont, L. Cazon, M. G. Cuesta, C. Gonzalez-Juanatey, J. Peteiro, N. Alvarez, M. Penas-Lado, A. Castro-Beiras, Mutation in the alpha-cardiac actin gene associated with apical hypertrophic cardiomyopathy, left ventricular non-compaction, and septal defects. *Eur Heart J* **28**, 1953-1961 (2007).
37. W. Song, E. Dyer, D. J. Stuckey, O. Copeland, M. C. Leung, C. Bayliss, A. Messer, R. Wilkinson, J. L. Tremoleda, M. D. Schneider, S. E. Harding, C. S. Redwood, K. Clarke, K. Nowak, L. Monserrat, D. Wells, S. B. Marston, Molecular mechanism of the E99K mutation in cardiac actin (ACTC Gene) that causes apical hypertrophy in man and mouse. *J Biol Chem* **286**, 27582-27593 (2011).
38. A. A. Geisterfer-Lowrance, M. Christe, D. A. Conner, J. S. Ingwall, F. J. Schoen, C. E. Seidman, J. G. Seidman, A mouse model of familial hypertrophic cardiomyopathy. *Science* **272**, 731-734 (1996).
39. C. M. Wolf, I. P. Moskowitz, S. Arno, D. M. Branco, C. Semsarian, S. A. Bernstein, M. Peterson, M. Maida, G. E. Morley, G. Fishman, C. I. Berul, C. E. Seidman, J. G. Seidman, Somatic events modify hypertrophic cardiomyopathy pathology and link hypertrophy to arrhythmia. *Proc Natl Acad Sci U S A* **102**, 18123-18128 (2005).

40. B. R. Ertz-Berger, H. He, C. Dowell, S. M. Factor, T. E. Haim, S. Nunez, S. D. Schwartz, J. S. Ingwall, J. C. Tardiff, Changes in the chemical and dynamic properties of cardiac troponin T cause discrete cardiomyopathies in transgenic mice. *Proc Natl Acad Sci U S A* **102**, 18219-18224 (2005).

41. S. Vakrou, Y. Liu, L. Zhu, G. V. Greenland, B. Simsek, V. B. Hebl, Y. Guan, K. Woldemichael, C. C. Talbot, M. A. Aon, R. Fukunaga, M. R. Abraham, Differences in molecular phenotype in mouse and human hypertrophic cardiomyopathy. *Sci Rep* **11**, 13163 (2021).

42. H. Nishimura, T. Okazaki, Y. Tanaka, K. Nakatani, M. Hara, A. Matsumori, S. Sasayama, A. Mizoguchi, H. Hiai, N. Minato, T. Honjo, Autoimmune dilated cardiomyopathy in PD-1 receptor-deficient mice. *Science* **291**, 319-322 (2001).

43. T. Okazaki, Y. Tanaka, R. Nishio, T. Mitsuiye, A. Mizoguchi, J. Wang, M. Ishida, H. Hiai, A. Matsumori, N. Minato, T. Honjo, Autoantibodies against cardiac troponin I are responsible for dilated cardiomyopathy in PD-1-deficient mice. *Nat Med* **9**, 1477-1483 (2003).

44. L. A. Kalekar, J. N. Cohen, N. Prevel, P. M. Sandoval, A. N. Mathur, J. M. Moreau, M. M. Lowe, A. Nosbaum, P. J. Wolters, A. Haemel, F. Boin, M. D. Rosenblum, Regulatory T cells in skin are uniquely poised to suppress profibrotic immune responses. *Sci Immunol* **4**, (2019).

45. H. Grasshoff, S. Comduhr, L. R. Monne, A. Muller, P. Lamprecht, G. Riemekasten, J. Y. Humrich, Low-Dose IL-2 Therapy in Autoimmune and Rheumatic Diseases. *Front Immunol* **12**, 648408 (2021).

46. C. Krieg, S. Letourneau, G. Pantaleo, O. Boyman, Improved IL-2 immunotherapy by selective stimulation of IL-2 receptors on lymphocytes and endothelial cells. *Proc Natl Acad Sci U S A* **107**, 11906-11911 (2010).

47. J. C. Tardiff, T. E. Hewett, B. M. Palmer, C. Olsson, S. M. Factor, R. L. Moore, J. Robbins, L. A. Leinwand, Cardiac troponin T mutations result in allele-specific phenotypes in a mouse model for hypertrophic cardiomyopathy. *J Clin Invest* **104**, 469-481 (1999).

48. J. James, Y. Zhang, H. Osinska, A. Sanbe, R. Klevitsky, T. E. Hewett, J. Robbins, Transgenic modeling of a cardiac troponin I mutation linked to familial hypertrophic cardiomyopathy. *Circ Res* **87**, 805-811 (2000).

49. R. Prabhakar, G. P. Boivin, I. L. Grupp, B. Hoit, G. Arteaga, R. J. Solaro, D. F. Wieczorek, A familial hypertrophic cardiomyopathy alpha-tropomyosin mutation causes severe cardiac hypertrophy and death in mice. *J Mol Cell Cardiol* **33**, 1815-1828 (2001).

50. S. C. Smith, P. M. Allen, Myosin-induced acute myocarditis is a T cell-mediated disease. *J Immunol* **147**, 2141-2147 (1991).

51. C. Gil-Cruz, C. Perez-Shibayama, A. De Martin, F. Ronchi, K. van der Borght, R. Niederer, L. Onder, M. Lutge, M. Novkovic, V. Nindl, G. Ramos, M. Arnoldini, E. M. C. Slack, V. Boivin-Jahns, R. Jahns, M. Wyss, C. Mooser, B. N. Lambrecht, M. T. Maeder, H. Rickli, L. Flatz, U. Eriksson, M. B. Geuking, K. D. McCoy, B. Ludewig, Microbiota-derived peptide mimics drive lethal inflammatory cardiomyopathy. *Science* **366**, 881-886 (2019).

52. M. K. D. Scott, K. Quinn, Q. Li, R. Carroll, H. Warsinske, F. Vallania, S. Chen, M. A. Carns, K. Aren, J. Sun, K. Koloms, J. Lee, J. Baral, J. Kropski, H. Zhao, E. Herzog, F. J. Martinez, B. B. Moore, M. Hinchcliff, J. Denny, N. Kaminski, J. D. Herazo-Maya, N. H. Shah, P. Khatri, Increased monocyte count as a cellular biomarker for poor outcomes in fibrotic diseases: a retrospective, multicentre cohort study. *Lancet Respir Med* **7**, 497-508 (2019).

53. S. S. Bansal, M. A. Ismahil, M. Goel, G. Zhou, G. Rokosh, T. Hamid, S. D. Prabhu, Dysfunctional and Proinflammatory Regulatory T-Lymphocytes Are Essential for Adverse Cardiac Remodeling in Ischemic Cardiomyopathy. *Circulation* **139**, 206-221 (2019).

54. J. Lee, D. Kim, B. Min, Tissue Resident Foxp3+ Regulatory T Cells: Sentinels and Saboteurs in Health and Disease. *Frontiers in Immunology* **13**, (2022).

55. S. A. Villalta, W. Rosenthal, L. Martinez, A. Kaur, T. Sparwasser, J. G. Tidball, M. Margeta, M. J. Spencer, J. A. Bluestone, Regulatory T cells suppress muscle inflammation and injury in muscular dystrophy. *Sci Transl Med* **6**, 258ra142 (2014).

56. N. Xia, Y. Lu, M. Gu, N. Li, M. Liu, J. Jiao, Z. Zhu, J. Li, D. Li, T. Tang, B. Lv, S. Nie, M. Zhang, M. Liao, Y. Liao, X. Yang, X. Cheng, A Unique Population of Regulatory T Cells in Heart Potentiates Cardiac Protection From Myocardial Infarction. *Circulation* **142**, 1956-1973 (2020).

57. S. Zacchigna, V. Martinelli, S. Moimas, A. Colliva, M. Anzini, A. Nordio, A. Costa, M. Rehman, S. Vodret, C. Pierro, G. Colussi, L. Zentilin, M. I. Gutierrez, E. Dirkx, C. Long, G. Sinagra, D. Klatzmann, M. Giacca, Paracrine effect of regulatory T cells promotes cardiomyocyte proliferation during pregnancy and after myocardial infarction. *Nat Commun* **9**, 2432 (2018).

58. Y. Shi, M. Fukuoka, G. Li, Y. Liu, M. Chen, M. Konviser, X. Chen, M. A. Opavsky, P. P. Liu, Regulatory T cells protect mice against coxsackievirus-induced myocarditis through the transforming growth factor beta-coxsackie-adenovirus receptor pathway. *Circulation* **121**, 2624-2634 (2010).

59. Y. Han, J. Lai, J. Tao, Y. Tai, W. Zhou, P. Guo, Z. Wang, M. Wang, Q. Wang, Sustaining Circulating Regulatory T Cell Subset Contributes to the Therapeutic Effect of Paroxetine on Mice With Diabetic Cardiomyopathy. *Circ J* **84**, 1587-1598 (2020).

60. H. Kvakan, M. Kleinewietfeld, F. Qadri, J. K. Park, R. Fischer, I. Schwarz, H. P. Rahn, R. Plehm, M. Wellner, S. Elitok, P. Gratze, R. Dechend, F. C. Luft, D. N. Muller, Regulatory T cells ameliorate angiotensin II-induced cardiac damage. *Circulation* **119**, 2904-2912 (2009).

61. P. Kanellakis, T. N. Dinh, A. Agrotis, A. Bobik, CD4(+)CD25(+)Foxp3(+) regulatory T cells suppress cardiac fibrosis in the hypertensive heart. *J Hypertens* **29**, 1820-1828 (2011).

62. Y. Lu, N. Xia, X. Cheng, Regulatory T Cells in Chronic Heart Failure. *Frontiers in Immunology* **12**, (2021).

63. E. J. Rowin, B. J. Maron, R. T. Carrick, P. P. Patel, B. Koethe, S. Wells, M. S. Maron, Outcomes in Patients With Hypertrophic Cardiomyopathy and Left Ventricular Systolic Dysfunction. *J Am Coll Cardiol* **75**, 3033-3043 (2020).

64. M. Chaffin, I. Papangeli, B. Simonson, A. D. Akkad, M. C. Hill, A. Arduini, S. J. Fleming, M. Melanson, S. Hayat, M. Kost-Alimova, O. Atwa, J. Ye, K. C. Bedi, Jr., M. Nahrendorf, V. K. Kaushik, C. M. Stegmann, K. B. Margulies, N. R. Tucker, P. T. Ellinor, Single-nucleus profiling of human dilated and hypertrophic cardiomyopathy. *Nature* **608**, 174-180 (2022).

65. X. Liu, K. Yin, L. Chen, W. Chen, W. Li, T. Zhang, Y. Sun, M. Yuan, H. Wang, Y. Song, S. Wang, S. Hu, Z. Zhou, Lineage-specific regulatory changes in hypertrophic cardiomyopathy unraveled by single-nucleus RNA-seq and spatial transcriptomics. *Cell Discov* **9**, 6 (2023).

66. I. Korsunsky, N. Millard, J. Fan, K. Slowikowski, F. Zhang, K. Wei, Y. Baglaenko, M. Brenner, P. R. Loh, S. Raychaudhuri, Fast, sensitive and accurate integration of single-cell data with Harmony. *Nat Methods* **16**, 1289-1296 (2019).

67. V. A. Traag, L. Waltman, N. J. van Eck, From Louvain to Leiden: guaranteeing well-connected communities. *Sci Rep* **9**, 5233 (2019).

68. F. A. Wolf, P. Angerer, F. J. Theis, SCANPY: large-scale single-cell gene expression data analysis. *Genome Biol* **19**, 15 (2018).

69. M. E. Ritchie, B. Phipson, D. Wu, Y. Hu, C. W. Law, W. Shi, G. K. Smyth, limma powers differential expression analyses for RNA-sequencing and microarray studies. *Nucleic Acids Res* **43**, e47 (2015).

70. G. S. Korotkevich, V.; Budin, N.; Shpak, B.; Artyomov, M. N.; Sergushichev, A., Fast gene set enrichment analysis. *bioRxiv*, (2021).

71. A. Subramanian, P. Tamayo, V. K. Mootha, S. Mukherjee, B. L. Ebert, M. A. Gillette, A. Paulovich, S. L. Pomeroy, T. R. Golub, E. S. Lander, J. P. Mesirov, Gene set enrichment analysis: a knowledge-based approach for interpreting genome-wide expression profiles. *Proc Natl Acad Sci U S A* **102**, 15545-15550 (2005).

72. A. Liberzon, A. Subramanian, R. Pinchback, H. Thorvaldsdottir, P. Tamayo, J. P. Mesirov, Molecular signatures database (MSigDB) 3.0. *Bioinformatics* **27**, 1739-1740 (2011).

73. S. Bohl, C. A. Lygate, H. Barnes, D. Medway, L. A. Stork, J. Schulz-Menger, S. Neubauer, J. E. Schneider, Advanced methods for quantification of infarct size in mice using three-dimensional high-field late gadolinium enhancement MRI. *Am J Physiol Heart Circ Physiol* **296**, H1200-1208 (2009).

74. M. Martin, Cutadapt Removes Adapter Sequences From High-Throughput Sequencing Reads. *EMBnet.journal* **17**, 10-12 (2011).
75. A. Dobin, C. A. Davis, F. Schlesinger, J. Drenkow, C. Zaleski, S. Jha, P. Batut, M. Chaisson, T. R. Gingeras, STAR: ultrafast universal RNA-seq aligner. *Bioinformatics* **29**, 15-21 (2013).
76. Y. Liao, G. K. Smyth, W. Shi, featureCounts: an efficient general purpose program for assigning sequence reads to genomic features. *Bioinformatics* **30**, 923-930 (2014).
77. R. C. Team., *R: A language and environment for statistical computing.*, R Foundation for Statistical Computing (Vienna, Austria, 2020).
78. W. Huber, V. J. Carey, R. Gentleman, S. Anders, M. Carlson, B. S. Carvalho, H. C. Bravo, S. Davis, L. Gatto, T. Girke, R. Gottardo, F. Hahne, K. D. Hansen, R. A. Irizarry, M. Lawrence, M. I. Love, J. MacDonald, V. Obenchain, A. K. Oles, H. Pages, A. Reyes, P. Shannon, G. K. Smyth, D. Tenenbaum, L. Waldron, M. Morgan, Orchestrating high-throughput genomic analysis with Bioconductor. *Nat Methods* **12**, 115-121 (2015).
79. M. D. Robinson, D. J. McCarthy, G. K. Smyth, edgeR: a Bioconductor package for differential expression analysis of digital gene expression data. *Bioinformatics* **26**, 139-140 (2010).
80. D. J. McCarthy, Y. Chen, G. K. Smyth, Differential expression analysis of multifactor RNA-Seq experiments with respect to biological variation. *Nucleic Acids Res* **40**, 4288-4297 (2012).
81. M. D. Robinson, A. Oshlack, A scaling normalization method for differential expression analysis of RNA-seq data. *Genome Biol* **11**, R25 (2010).
82. K. L. Thomson, E. Ormondroyd, A. R. Harper, T. Dent, K. McGuire, J. Baksi, E. Blair, P. Brennan, R. Buchan, T. Bueser, C. Campbell, G. Carr-White, S. Cook, M. Daniels, S. V. V. Deevi, J. Goodship, J. B. G. Hayesmoore, A. Henderson, T. Lamb, S. Prasad, P. Rayner-Matthews, L. Robert, L. Sneddon, H. Stark, R. Walsh, J. S. Ware, M. Farrall, H. C. Watkins, N. B.-R. D. Consortium, Analysis of 51 proposed hypertrophic cardiomyopathy genes from genome sequencing data in sarcomere negative cases has negligible diagnostic yield. *Genet Med* **21**, 1576-1584 (2019).
83. G. X. Zheng, J. M. Terry, P. Belgrader, P. Ryvkin, Z. W. Bent, R. Wilson, S. B. Ziraldo, T. D. Wheeler, G. P. McDermott, J. Zhu, M. T. Gregory, J. Shuga, L. Montesclaros, J. G. Underwood, D. A. Masquelier, S. Y. Nishimura, M. Schnall-Levin, P. W. Wyatt, C. M. Hindson, R. Bharadwaj, A. Wong, K. D. Ness, L. W. Beppu, H. J. Deeg, C. McFarland, K. R. Loeb, W. J. Valente, N. G. Ericson, E. A. Stevens, J. P. Radich, T. S. Mikkelsen, B. J. Hindson, J. H. Bielas, Massively parallel digital transcriptional profiling of single cells. *Nat Commun* **8**, 14049 (2017).
84. M. D. Young, S. Behjati, SoupX removes ambient RNA contamination from droplet-based single-cell RNA sequencing data. *Gigascience* **9**, (2020).
85. C. S. McGinnis, L. M. Murrow, Z. J. Gartner, DoubletFinder: Doublet Detection in Single-Cell RNA Sequencing Data Using Artificial Nearest Neighbors. *Cell Syst* **8**, 329-337 e324 (2019).
86. Y. Hao, S. Hao, E. Andersen-Nissen, W. M. Mauck, 3rd, S. Zheng, A. Butler, M. J. Lee, A. J. Wilk, C. Darby, M. Zager, P. Hoffman, M. Stoeckius, E. Papalexi, E. P. Mimitou, J. Jain, A. Srivastava, T. Stuart, L. M. Fleming, B. Yeung, A. J. Rogers, J. M. McElrath, C. A. Blish, R. Gottardo, P. Smibert, R. Satija, Integrated analysis of multimodal single-cell data. *Cell* **184**, 3573-3587 e3529 (2021).
87. A. M. Hadi, K. T. Mouchaers, I. Schalij, K. Grunberg, G. A. Meijer, A. Vonk-Noordegraaf, W. J. van der Laarse, J. A. Belien, Rapid quantification of myocardial fibrosis: a new macro-based automated analysis. *Cell Oncol (Dordr)* **34**, 343-354 (2011).
88. T. Thomas, M. Friedrich, C. Rich-Griffin, M. Pohin, D. Agarwal, J. Pakpoor, C. Lee, R. Tandon, A. Rendek, D. Aschenbrenner, A. Jainarayanan, A. Voda, J. H. Y. Siu, R. Sanches-Peres, E. Nee, D. Sathananthan, D. Kotliar, P. Todd, M. Kiourlappou, L. Gartner, N. Ilott, F. Issa, J. Hester, J. Turner, S. Nayar, J. Mackerodt, F. Zhang, A. Jonsson, M. Brenner, S. Raychaudhuri, R. Kulicke, D. Ramsdell, N. Stransky, R. Pagliarini, P. Bielecki, N. Spies, B. Marsden, S. Taylor, A. Wagner, P. Klenerman, A. Walsh, M. Coles, L. Jostins-Dean, F. M. Powrie, A. Filer, S. Travis, H. H. Uhlig, C. A. Dendrou, C. D. Buckley, A longitudinal single-cell atlas of anti-tumour necrosis factor treatment in inflammatory bowel disease. *Nat Immunol* **25**, 2152-2165 (2024).

Acknowledgments:

We thank Drs. H. Lockstone, A. Taylor, and B. Wright for processing some of the bulk RNA-seq data, Dr. R. Montandon from the Flow Cytometry Facility for providing cell sorting service, and Mr. E. Drydale and Dr. J. Bancroft from the Cellular Imaging Core Facility for imaging analysis service (University of Oxford, Centre for Human Genetics). We are grateful to Prof. F. Powrie for providing the *Rag-1*^{KO} mice as a gift. We also thank CSC-Oxford funding (China Scholarship Council – University of Oxford, under number SFF2122_CSCUO_1284663/202108330024) to support Siwei' DPhil study.

Funding:

This work was funded by the British Heart Foundation (RG/18/9/33887 to HA, CR, and HW and CH/1992001/6764 to HW) and supported by the BHF Centre for Research Excellence in Oxford. J.G. Seidman, C.E. Seidman and H. Watkins are supported by the British Heart Foundation's Big Beat Challenge award to CureHeart (BBC/F/21/220106 to JGS, JES, and HW).

Author contributions:

YJW, HA, CR, and HW conceived the study and designed the experiments. HA, CR, and HW provided the funding. JCL and EJS acquired clinical data and clinic specimens for immunohistochemistry. KS, ABL, BS, JB, MK, and AB performed cardiac phenotyping. YJW, KS, and ABL conducted flow cytometry and cytokine/chemokine profiling. YJW, KS, ABL, AB, JCKF, and AH performed tissue staining and fibrosis analysis. YJW, BS, MS, and CDB designed and performed Cell-DIVE staining. YJW, LAS, MLM, and JES designed and performed LGE-MRI animal experiments. YJW and KS generated samples for CITE-seq animal experiments, processed by MA. SM and CR generated the *Actc1*^{E99K} mouse model. YJW, SD, and CAD analysed bulk RNA-seq and CITE-seq data from animal models and human snRNA seq data. JES and JGS provided bulk RNA seq data from two *αMhc* HCM animal models. YJW, HA, CR, and HW wrote and revised the manuscript. All authors reviewed the manuscript.

Competing interests: All authors declare that they have no competing interests.

Data and materials availability: All data associated with this study are present in the paper or supplementary materials. Human and mouse tissue samples will not be provided unless a Material Transfer Agreement (MTA) is fully executed. Bulk and single cell gene expression data are available from the National Center for Biotechnology Information (NCBI) under Bioproject PRJNA973875. No custom scripts have been generated or used in the study.

Figure legends

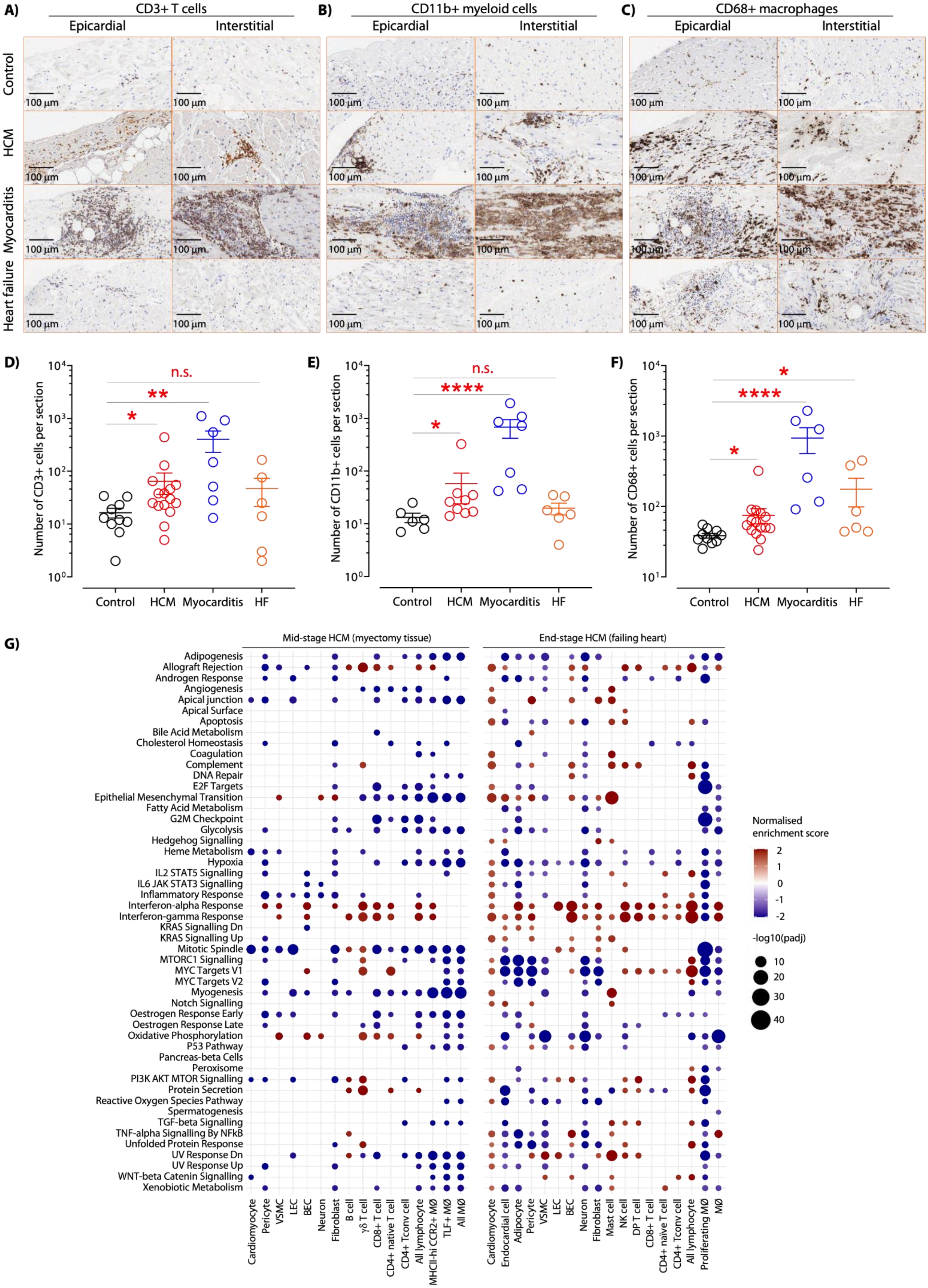
A)
CD3+ T cells
Epicardial
Interstitial
B)
CD11b+ myeloid cells
Epicardial
Interstitial
C)
CD68+ macrophages
Epicardial
Interstitial
Control
HCM
Myocarditis
Heart failure
100 μm
D)
Number of CD3+ cells per section
10^0
10^1
10^2
10^3
10^4
n.s.
**
*
Control
HCM
Myocarditis
HF
E)
Number of CD11b+ cells per section
n.s.
****
*
Control
HCM
Myocarditis
HF
F)
Number of CD68+ cells per section
*
****
*
Control
HCM
Myocarditis
HF
G)
Mid-stage HCM (myectomy tissue)
End-stage HCM (failing heart)
Adipogenesis
Allograft Rejection
Androgen Response
Angiogenesis
Apical junction
Apical Surface
Apoptosis
Bile Acid Metabolism
Cholesterol Homeostasis
Coagulation
Complement
DNA Repair
E2F Targets
Epithelial Mesenchymal Transition
Fatty Acid Metabolism
G2M Checkpoint
Glycolysis
Hedgehog Signalling
Heme Metabolism
Hypoxia
IL2 STAT5 Signalling
IL6 JAK STAT3 Signalling
Inflammatory Response
Interferon-alpha Response
Interferon-gamma Response
KRAS Signalling Dn
KRAS Signalling Up
Mitotic Spindle
MTORC1 Signalling
MYC Targets V1
MYC Targets V2
Myogenesis
Notch Signalling
Oestrogen Response Early
Oestrogen Response Late
Oxidative Phosphorylation
P53 Pathway
Pancreas-beta Cells
Peroxisome
PI3K AKT MTOR Signalling
Protein Secretion
Reactive Oxygen Species Pathway
Spermatogenesis
TGF-beta Signalling
TNF-alpha Signalling By NFkB
Unfolded Protein Response
UV Response Dn
UV Response Up
WNT-beta Catenin Signalling
Xenobiotic Metabolism
Cardiomyocyte
Pericyte
VSMC
LEC
BEC
Neuron
Fibroblast
B cell
γδ T cell
CD8+ T cell
CD4+ native T cell
CD4+ Tconv cell
All lymphocyte
MHCII-hi CCR2+ MØ
TLF+ MØ
All MØ
Cardiomyocyte
Endocardial cell
Adipocyte
Pericyte
VSMC
LEC
BEC
Neuron
Fibroblast
Mast cell
NK cell
DP T cell
CD8+ T cell
CD4+ naïve T cell
CD4+ Tconv cell
All lymphocyte
Proliferating MØ
MØ
Normalised enrichment score
2
1
0
-1
-2
-log10(padj)
10
20
30
40

Figure 1. Focal infiltration and chronic inflammation in HCM human hearts. The study includes post-mortem or explanted hearts from healthy controls (n=10), patients with HCM (n=16), myocarditis (n=7), and heart failure (n=6). Hearts were stained for **(A)** CD3$^+$ T cells, **(B)** CD11b$^+$ myeloid cells, and **(C)** CD68$^+$ macrophages, with representative images from epicardial and interstitial areas. Scale bar represents 100 µm. **(D-F)** Immune cell quantification is shown, based on at least 10 image sections per sample. Data are shown in mean ± SEM and statistical analysis used one-way ANOVA with Kruskal-Wallis test: two-stage step-up method of Benjamini, Krieger and Yekutieli (adjusted *p*-values ∗: < 0.05, ∗∗: < 0.01, ∗∗∗∗: < 0.0001). **(G)** Two publicly available snRNA-seq data sets were recruited, including 1) patients with mid-stage HCM underwent myectomy and healthy donors and 2) patients with late-stage HCM with failing hearts and non-failing individuals. Changes of gene expression in hallmark gene sets in GSEA, which represent 50 well-defined biological processes, were measured in normalised enrichment scores and visualized as nodes with various colors and sizes. Color intensity reflects the direction and strength of regulation, where darker red represents stronger upregulation and darker blue represents stronger downregulation. Node sizes indicate the degree of statistical significance, where a larger size indicates greater statistical significance. All displayed nodes are statistically significant (*p*-value < 0.05). (VSMC: vascular smooth muscle cells; LEC: lymphatic endothelial cells; BEC: blood endothelial cells; *CD4*+ Tconv cells: *CD4*+ conventional T cells; DP T cell: *CD4*+ *CD8*+ double positive T cells; TLF+ MØ: *TIMD4*+ / *LYVE-1*+ / *FOLR2*+ resident macrophages).

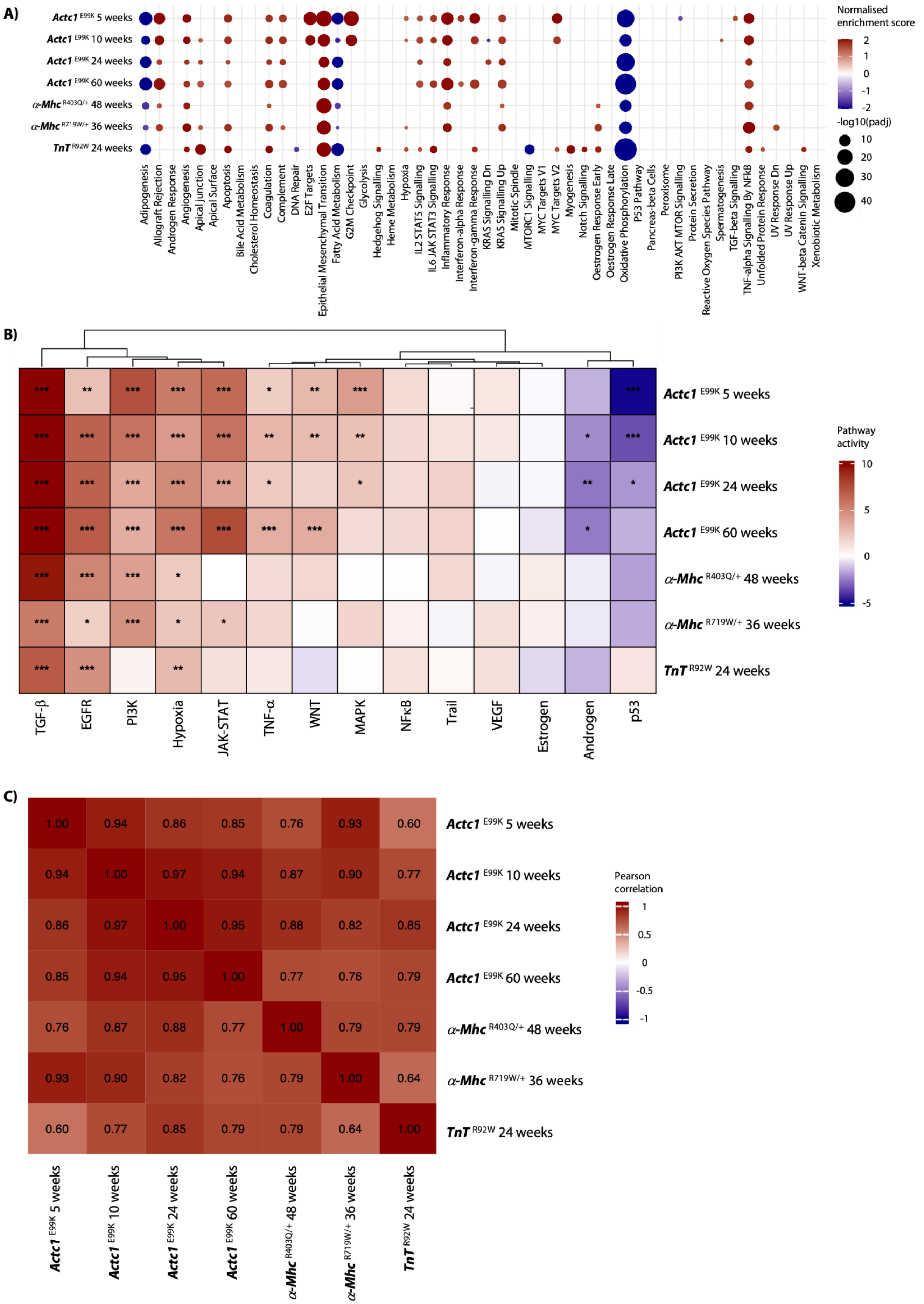
A)
Actc1 E99K 5 weeks
Actc1 E99K 10 weeks
Actc1 E99K 24 weeks
Actc1 E99K 60 weeks
α-Mhc R403Q/+ 48 weeks
α-Mhc R719W/+ 36 weeks
TnT R92W 24 weeks
Adipogenesis
Allograft Rejection
Androgen Response
Angiogenesis
Apical Junction
Apical Surface
Apoptosis
Bile Acid Metabolism
Cholesterol Homeostasis
Coagulation
Complement
DNA Repair
E2F Targets
Epithelial Mesenchymal Transition
Fatty Acid Metabolism
G2M Checkpoint
Glycolysis
Hedgehog Signalling
Heme Metabolism
Hypoxia
IL2 STAT5 Signalling
IL6 JAK STAT3 Signalling
Inflammatory Response
Interferon-alpha Response
Interferon-gamma Response
KRAS Signalling Dn
KRAS Signalling Up
Mitotic Spindle
MTORC1 Signalling
MYC Targets V1
MYC Targets V2
Myogenesis
Notch Signalling
Oestrogen Response Early
Oestrogen Response Late
Oxidative Phosphorylation
P53 Pathway
Pancreas-beta Cells
Peroxisome
PI3K AKT MTOR Signalling
Protein Secretion
Reactive Oxygen Species Pathway
Spermatogenesis
TGF-beta Signalling
TNF-alpha Signalling By NFkB
Unfolded Protein Response
UV Response Dn
UV Response Up
WNT-beta Catenin Signalling
Xenobiotic Metabolism
Normalised enrichment score
2
1
0
-1
-2
-log10(padj)
10
20
30
40
B)
Actc1 E99K 5 weeks
Actc1 E99K 10 weeks
Actc1 E99K 24 weeks
Actc1 E99K 60 weeks
α-Mhc R403Q/+ 48 weeks
α-Mhc R719W/+ 36 weeks
TnT R92W 24 weeks
TGF-β
EGFR
PI3K
Hypoxia
JAK-STAT
TNF-α
WNT
MAPK
NFκB
Trail
VEGF
Estrogen
Androgen
p53
Pathway activity
10
5
0
-5
C)
1.00 0.94 0.86 0.85 0.76 0.93 0.60 Actc1 E99K 5 weeks
0.94 1.00 0.97 0.94 0.87 0.90 0.77 Actc1 E99K 10 weeks
0.86 0.97 1.00 0.95 0.88 0.82 0.85 Actc1 E99K 24 weeks
0.85 0.94 0.95 1.00 0.77 0.76 0.79 Actc1 E99K 60 weeks
0.76 0.87 0.88 0.77 1.00 0.79 0.79 α-Mhc R403Q/+ 48 weeks
0.93 0.90 0.82 0.76 0.79 1.00 0.64 α-Mhc R719W/+ 36 weeks
0.60 0.77 0.85 0.79 0.79 0.64 1.00 TnT R92W 24 weeks
Actc1 E99K 5 weeks
Actc1 E99K 10 weeks
Actc1 E99K 24 weeks
Actc1 E99K 60 weeks
α-Mhc R403Q/+ 48 weeks
α-Mhc R719W/+ 36 weeks
TnT R92W 24 weeks
Pearson correlation
1
0.5
0
-0.5
-1

Figure 2. Similar RNA signature across four HCM mouse models. (A) Bulk RNA-seq data sets from four HCM mouse models were recruited: 1) *Actc1*^{E99K} (5, 10, 24, 60 weeks, n=6-12 for each time point & genotype), 2) *αMhc* $^{R403Q/+}$ (48 weeks: n=8-9 for each genotype), 3) *αMhc* $^{R719W/+}$ (36 weeks: n=5-9 for each genotype), and 4) *TnT* ^{R92W} (24 weeks: n=3 for each genotype). Changes of gene expression in hallmark gene sets in GSEA, which represent 50 well-defined biological processes, were measured in normalised enrichment scores and visualized as nodes with various colors and sizes. Color intensity reflects the direction and strength of regulation, where darker red represents stronger upregulation and darker blue represents stronger downregulation. Node sizes indicate the degree of statistical significance, where a larger size indicates greater statistical significance. All displayed nodes are statistically significant (p-value < 0.05). **(B)** Changes of pathway activity of 14 biological processes were analyzed by PROGENy scores and visualized as a heatmap. Color intensity reflects the direction and strength of pathway activity, where darker red represents stronger upregulation (up to +10) and darker blue represents stronger downregulation (down to -5). Statistical analyses used t-test (p-values: $*$: < 0.05, $**$: < 0.01, $***$: < 0.001). **(C)** PROGENy scores were compared using Pearson Correlation to assess similarity between groups.

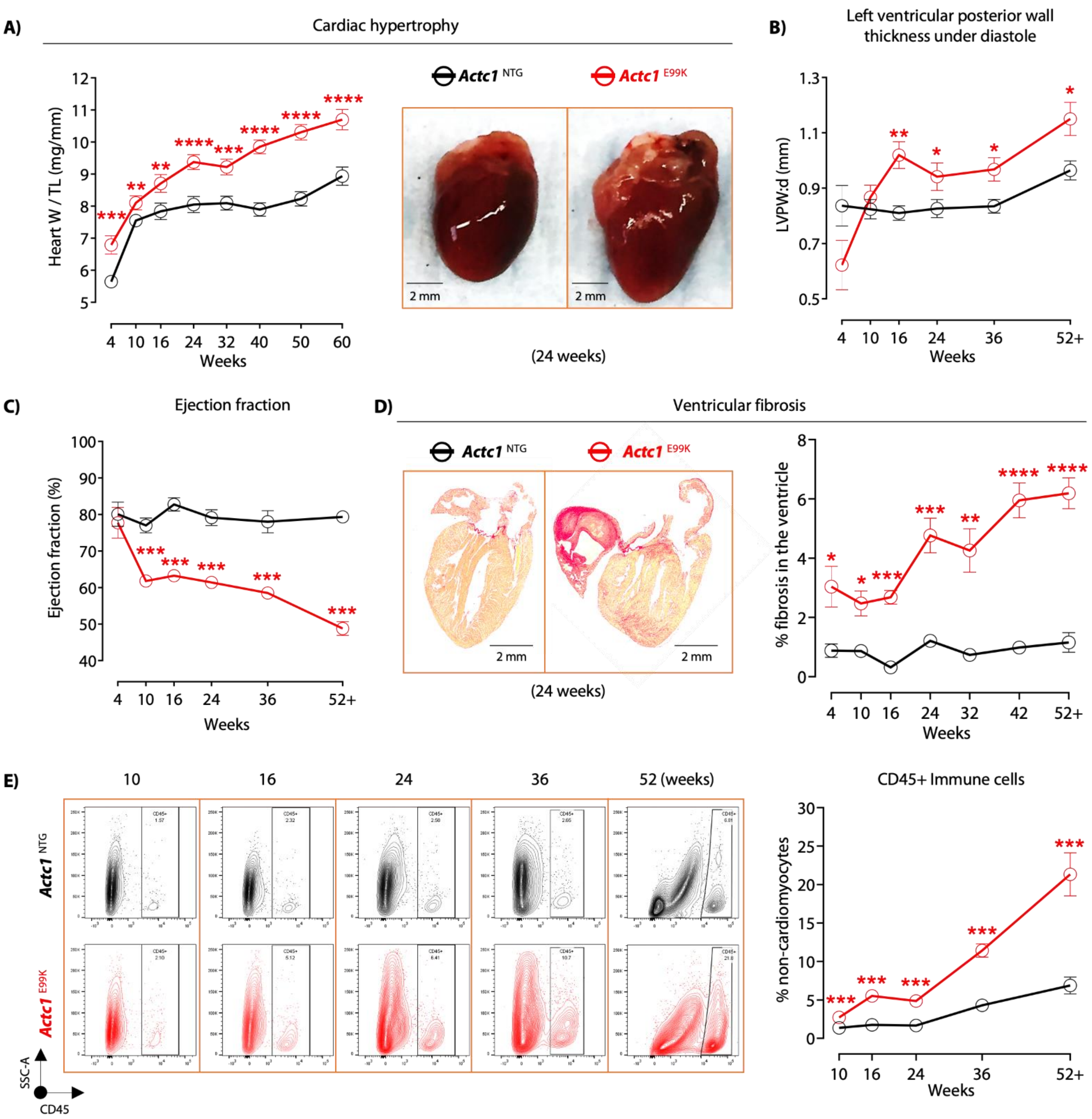
A)
Cardiac hypertrophy
Heart W / TL (mg/mm)
12
11
10
9
8
7
6
5
4
10
16
24
32
40
50
60
Weeks
***
**
**
****
***
****
****
****
Actc1 NTG
Actc1 E99K
2 mm
2 mm
(24 weeks)
B)
Left ventricular posterior wall thickness under diastole
LVPW:d (mm)
1.3
1.1
0.9
0.7
0.5
4
10
16
24
36
52+
Weeks
**
*
*
*
C)
Ejection fraction
Ejection fraction (%)
100
90
80
70
60
50
40
4
10
16
24
36
52+
Weeks
***
***
***
***
***
D)
Ventricular fibrosis
Actc1 NTG
Actc1 E99K
2 mm
2 mm
(24 weeks)
% fibrosis in the ventricle
8
6
4
2
0
4
10
16
24
32
42
52+
Weeks
*
*
***
***
**
****
****
E)
10
16
24
36
52 (weeks)
Actc1 NTG
Actc1 E99K
CD45+ 1.57
CD45+ 2.32
CD45+ 2.58
CD45+ 2.65
CD45+ 6.81
CD45+ 2.10
CD45+ 5.12
CD45+ 6.41
CD45+ 10.7
CD45+ 21.8
SSC-A
CD45
CD45+ Immune cells
% non-cardiomyocytes
30
25
20
15
10
5
0
10
16
24
36
52+
Weeks
***
***
***
***
***

Figure 3. Relationship between immune cells and progressive remodeling in *Actc1*$^{\text{E99K}}$ hearts. (A) Cardiac hypertrophy was longitudinally assessed by the heart weight/tibia length ratio ($n \geq 8$). Representative images show representative hearts from *Actc1*$^{\text{NTG}}$ and *Actc1*$^{\text{E99K}}$ mice at 24 weeks. Scale bar represents 2 mm. **(B)** LVPW: d and **(C)** EF% values are shown in a time-dependent manner in *Actc1*$^{\text{E99K}}$ mice ($n \geq 5$). **(D)** Ventricular fibrosis was longitudinally measured as percentage of collagen deposition in regions ($n \geq 4$), with representative images showing LV and apical fibrosis in *Actc1*$^{\text{E99K}}$ hearts at 24 weeks. Scale bar represents 50 µm. **(E)** CD45^{+} immune cells were analyzed by flow cytometry, presented as % live non-cardiomyocytes ($n \geq 7$). Data are shown in mean ± SEM and statistical analyses used two-way ANOVA with mixed-effects analysis: two-stage step-up method of Benjamini, Krieger and Yekutieli (adjusted *p*-values: ∗: < 0.05, ∗∗: < 0.01, ∗∗∗: < 0.001, ∗∗∗∗: < 0.0001).

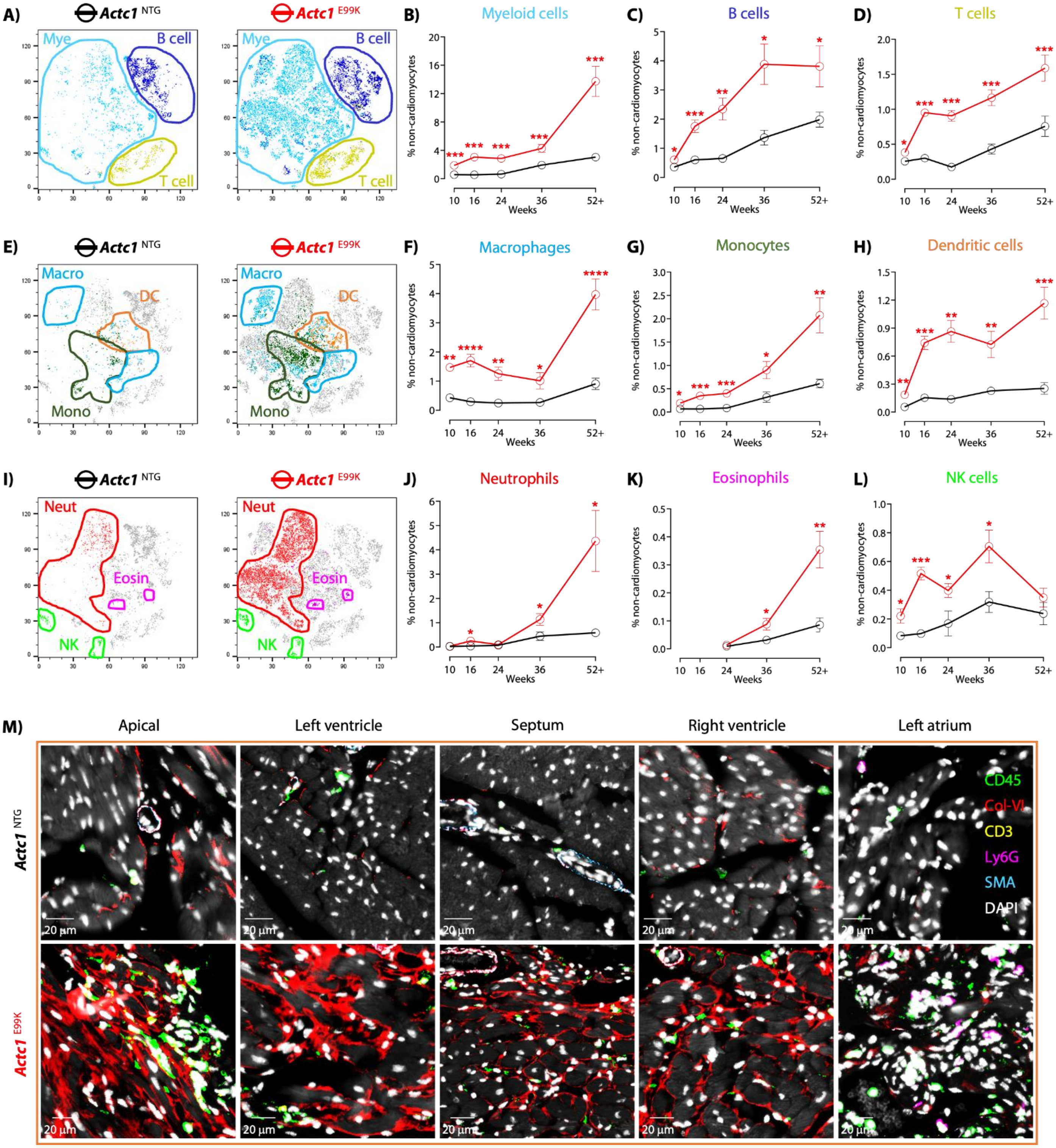
A)
Actc1 NTG
Actc1 E99K
Mye
B cell
T cell
B)
Myeloid cells
C)
B cells
D)
T cells
% non-cardiomyocytes
Weeks
10 16 24 36 52+
E)
Macro
DC
Mono
F)
Macrophages
G)
Monocytes
H)
Dendritic cells
I)
Neut
Eosin
NK
J)
Neutrophils
K)
Eosinophils
L)
NK cells
M)
Apical
Left ventricle
Septum
Right ventricle
Left atrium
CD45
Col-VI
CD3
Ly6G
SMA
DAPI
20 µm

Figure 4. Dynamic immune profile in *Actc1*$^{\mathrm{E99K}}$ hearts. (A) High-dimensional tSNE plots visualized changes in **(B)** myeloid cells, **(C**) B and **(D)** T lymphocytes, along with **(E)** mononuclear cells, including **(F)** macrophages, **(G)** monocytes, and **(H)** dendritic cells (DC), and **(I)** granulocytes, including **(J)** neutrophils and **(K)** eosinophils, and **(L)** natural killer cells ($n \geq 3$). Data are shown in mean ± SEM and statistical analyses used two-way ANOVA with mixed-effects analysis: two-stage step-up method of Benjamini, Krieger and Yekutieli (adjusted *p*-values: ∗: < 0.05, ∗∗: < 0.01, ∗∗∗: < 0.001, ∗∗∗∗: < 0.0001). **(M)** The Cell DIVE system captured cardiac collagen VI (red), SMA+ vascular smooth muscle cells (cyan), and CD45+ immune cells (green), including CD3+ T cells (yellow) and Ly6G+ neutrophils (magenta). Scale bar represents 20 μm. Representative images from of 36+ week-old *Actc1*$^{\mathrm{NTG}}$ (n=10) and *Actc1*$^{\mathrm{E99K}}$ (n=12) littermates.

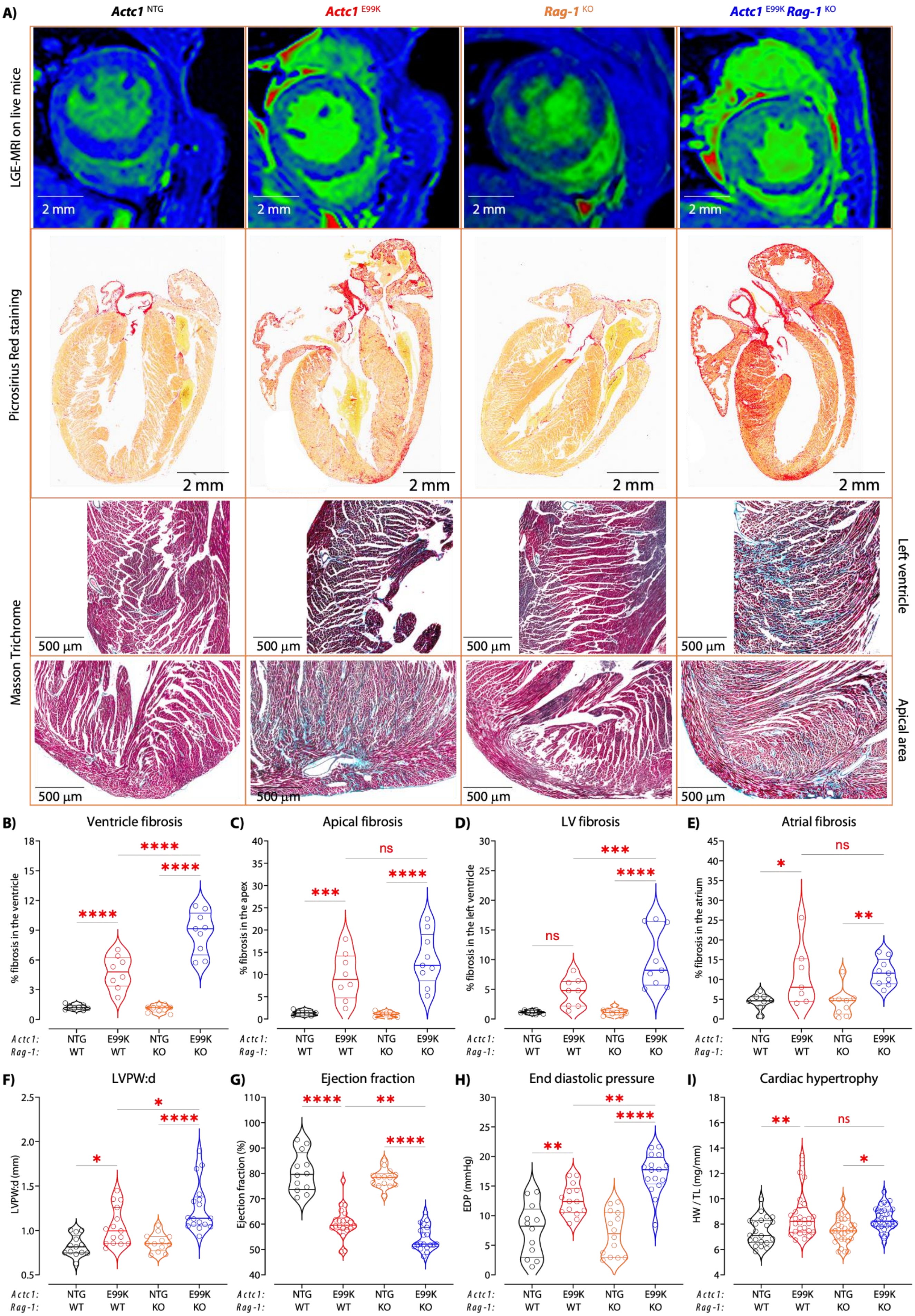
A)
Actc1 NTG
Actc1 E99K
Rag-1 KO
Actc1 E99K Rag-1 KO
LGE-MRI on live mice
2 mm
Picrosirius Red staining
2 mm
Masson Trichrome
500 µm
Left ventricle
Apical area
B) Ventricle fibrosis
% fibrosis in the ventricle
C) Apical fibrosis
% fibrosis in the apex
D) LV fibrosis
% fibrosis in the left ventricle
E) Atrial fibrosis
% fibrosis in the atrium
F) LVPW:d
LVPW:d (mm)
G) Ejection fraction
Ejection fraction (%)
H) End diastolic pressure
EDP (mmHg)
I) Cardiac hypertrophy
HW / TL (mg/mm)
Actc1: NTG E99K NTG E99K
Rag-1: WT WT KO KO
****
***
**
*
ns

Figure 5. Worsen cardiac fibrosis and dysfunction in *Actc1*$^{\mathbf{E99K}}$ hearts without lymphocytes. (A) Diffusive cardiac interstitial fibrosis in ventricles was shown in a short-axis view using LGE-CMR imaging on live mice (n=5-6). Blue represents a weak LGE signal whereas red reflects a strong LGE signal. Scale bar represents 2 mm. Cardiac fibrosis in a long-axis view was revealed by using Picrosirius Red or Masson Trichrome staining (n=8-9) on FFPE hearts from: *Actc1*$^{\text{NTG}}$, *Actc1*$^{\text{E99K}}$, *Rag-1*$^{\text{KO}}$, and *Actc1*$^{\text{E99K}}$ *Rag-1*$^{\text{KO}}$ mice at 24 weeks. Scale bar represents 50 μm in Picrosirius Red staining and 500 μm in Masson Trichrome staining, respectively. Percentages of fibrosis in marked sub-areas of the heart are shown using samples with Picrosirius Red staining (n=8-9). Percentage of fibrosis in **(B)** total ventricular area (including apical, LV, septum, and right ventricle), **(C)** apical, **(D)** LV, and **(E)** atria (including left and right atrium) are shown. **(F)** LV wall thickness and **(G)** EF% measured by echocardiography (n≥12), and **(H)** end diastolic pressure assessed by haemodynamic studies are shown (n≥12). **(I)** Cardiac hypertrophy is presented by the heart weight/tibia length ratio (n≥21). Data are shown in mean ± SEM and statistical analyses used one-way ANOVA with multiple comparison: Šidák (adjusted *p*-values: ∗: < 0.05, ∗∗: < 0.01, ∗∗∗: < 0.001, ∗∗∗∗: < 0.0001).

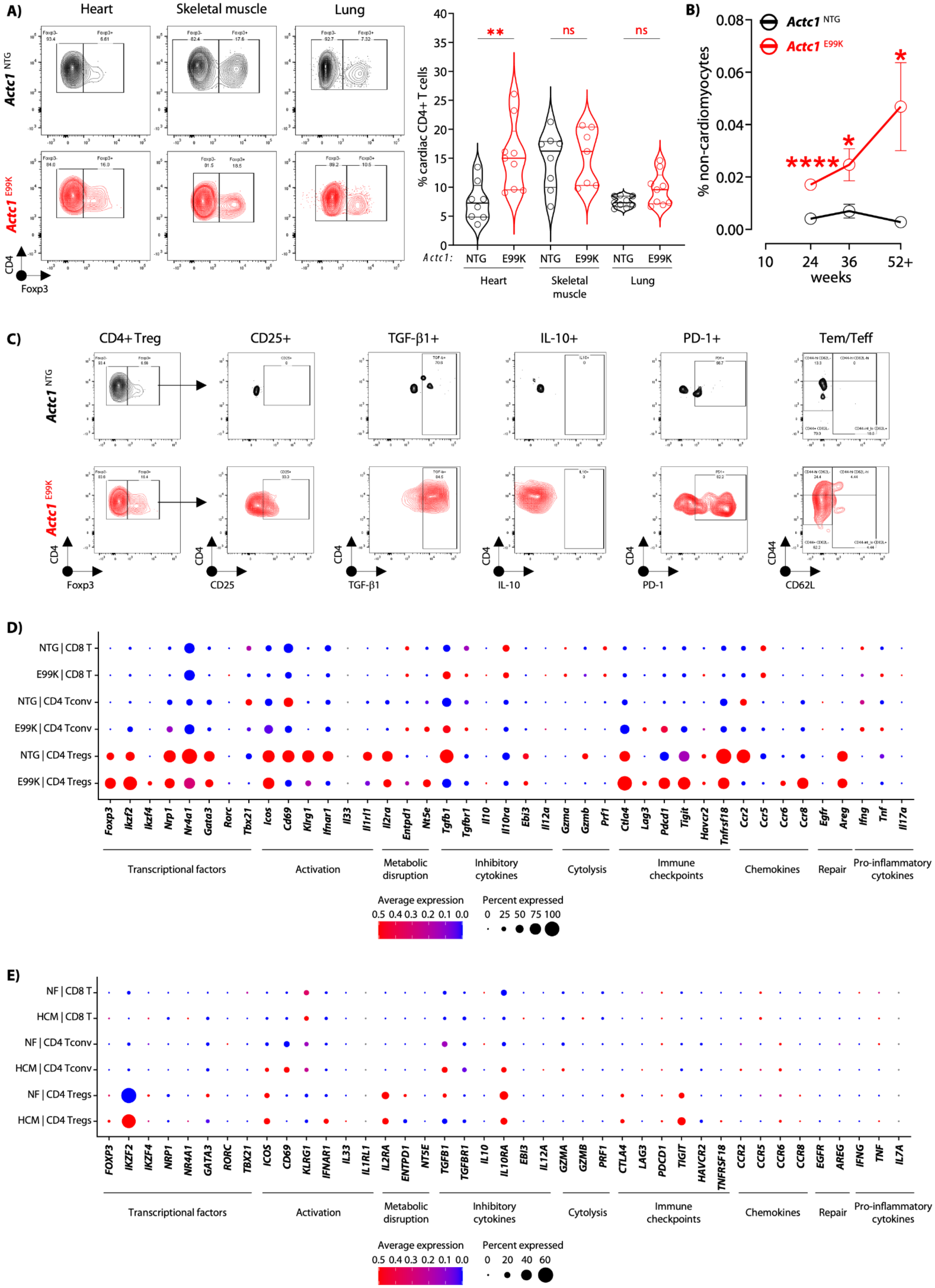
A)
Heart
Skeletal muscle
Lung
Actc1 NTG
Actc1 E99K
CD4
Foxp3
% cardiac CD4+ T cells
**
ns
ns
Actc1:
NTG
E99K
NTG
E99K
NTG
E99K
Heart
Skeletal muscle
Lung
B)
Actc1 NTG
Actc1 E99K
% non-cardiomyocytes
****
*
*
10
24
36
52+
weeks
C)
CD4+ Treg
CD25+
TGF-β1+
IL-10+
PD-1+
Tem/Teff
Actc1 NTG
Actc1 E99K
CD4
Foxp3
CD25
TGF-β1
IL-10
PD-1
CD44
CD62L
D)
NTG | CD8 T
E99K | CD8 T
NTG | CD4 Tconv
E99K | CD4 Tconv
NTG | CD4 Tregs
E99K | CD4 Tregs
Foxp3
Ikzf2
Ikzf4
Nrp1
Nr4a1
Gata3
Rorc
Tbx21
Icos
Cd69
Klrg1
Ifnar1
Il33
Il1rl1
Il2ra
Entpd1
Nt5e
Tgfb1
Tgfbr1
Il10
Il10ra
Ebi3
Il12a
Gzma
Gzmb
Prf1
Ctla4
Lag3
Pdcd1
Tigit
Havcr2
Tnfrsf18
Ccr2
Ccr5
Ccr6
Ccr8
Egfr
Areg
Ifng
Tnf
Il17a
Transcriptional factors
Activation
Metabolic disruption
Inhibitory cytokines
Cytolysis
Immune checkpoints
Chemokines
Repair
Pro-inflammatory cytokines
Average expression
0.5 0.4 0.3 0.2 0.1 0.0
Percent expressed
0 25 50 75 100
E)
NF | CD8 T
HCM | CD8 T
NF | CD4 Tconv
HCM | CD4 Tconv
NF | CD4 Tregs
HCM | CD4 Tregs
FOXP3
IKZF2
IKZF4
NRP1
NR4A1
GATA3
RORC
TBX21
ICOS
CD69
KLRG1
IFNAR1
IL33
IL1RL1
IL2RA
ENTPD1
NT5E
TGFB1
TGFBR1
IL10
IL10RA
EBI3
IL12A
GZMA
GZMB
PRF1
CTLA4
LAG3
PDCD1
TIGIT
HAVCR2
TNFRSF18
CCR2
CCR5
CCR6
CCR8
EGFR
AREG
IFNG
TNF
IL7A
Transcriptional factors
Activation
Metabolic disruption
Inhibitory cytokines
Cytolysis
Immune checkpoints
Chemokines
Repair
Pro-inflammatory cytokines
Average expression
0.5 0.4 0.3 0.2 0.1 0.0
Percent expressed
0 20 40 60

Figure 6. Enrichment of functionally altered Foxp3$^+$ Tregs in HCM hearts. **(A)** Percentages of Foxp3$^+$ Tregs among CD4$^+$ T cells in the heart, skeletal muscle, and lung of *Actc1*$^{\mathrm{NTG}}$ and *Actc1*$^{\mathrm{E99K}}$ mice are shown (n=7-9). Representative flow cytometric plots are illustrated. Data are shown in mean ± SEM and statistical analyses used one-way ANOVA with multiple comparison: Šidák (adjusted *p*-value: ∗∗: < 0.01). **(B)** Time-dependent changes of percentage of Foxp3$^+$ Tregs among CD4$^+$ T cells in the heart are presented ($n \geq 3$). Data are shown in mean ± SEM and statistical analyses used two-way ANOVA with mixed-effects analysis: two-stage step-up method of Benjamini, Krieger and Yekutieli (adjusted *p*-values: ∗: < 0.05, ∗∗∗∗: < 0.0001). **(C)** Immunosuppressive activities, including surface (CD25 and PD-1) and intracellular (TGF-β1 and IL-10) markers, and activation status, differentiation state, and migratory potential, classified by using CD44 and CD62L expression, are shown on cardiac Foxp3$^+$ CD4$^+$ Tregs from *Actc1*$^{\mathrm{NTG}}$ and *Actc1*$^{\mathrm{E99K}}$ mice ($n \geq 7$). **(D)** CD4$^+$ Foxp3$^+$ Tregs, CD4$^+$ (Tconv), and CD8$^+$ T cells from *Actc1*$^{\mathrm{NTG}}$ and *Actc1*$^{\mathrm{E99K}}$ hearts (n=3) were characterized using nine categories. Differential expressions of genes within individual categories are shown by nodes with different colors and sizes. Node size indicates the percentage of cells with positive expression. Brighter red represents a higher average expression. **(E)** Cardiac Tregs, Tconv, and CD8$^+$ T cells from patients with late-stage HCM (n=15) and non-failing controls (n=16) were characterized in a similar approach.

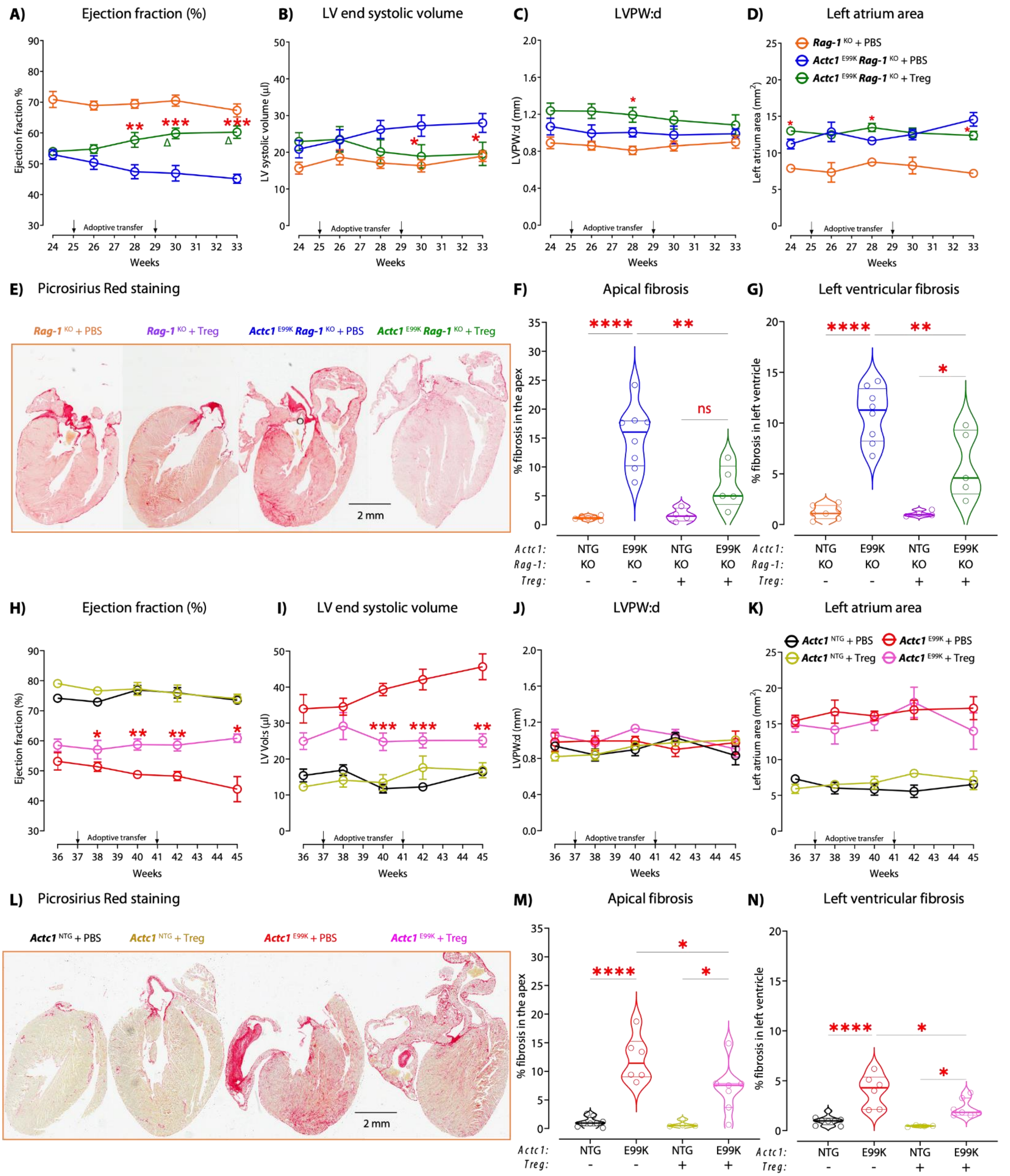
A) Ejection fraction (%)
Ejection fraction %
Adoptive transfer
Weeks
B) LV end systolic volume
LV systolic volume (µl)
C) LVPW:d
LVPW:d (mm)
D) Left atrium area
Left atrium area (mm²)
Rag-1 KO + PBS
Actc1 E99K Rag-1 KO + PBS
Actc1 E99K Rag-1 KO + Treg
E) Picrosirius Red staining
Rag-1 KO + PBS
Rag-1 KO + Treg
Actc1 E99K Rag-1 KO + PBS
Actc1 E99K Rag-1 KO + Treg
2 mm
F) Apical fibrosis
% fibrosis in the apex
****
**
ns
G) Left ventricular fibrosis
% fibrosis in left ventricle
****
**
*
Actc1: NTG E99K NTG E99K
Rag-1: KO KO KO KO
Treg: - - + +
H) Ejection fraction (%)
Ejection fraction (%)
I) LV end systolic volume
LV Vol;s (µl)
J) LVPW:d
LVPW;d (mm)
K) Left atrium area
Left atrium area (mm²)
Actc1 NTG + PBS
Actc1 E99K + PBS
Actc1 NTG + Treg
Actc1 E99K + Treg
L) Picrosirius Red staining
Actc1 NTG + PBS
Actc1 NTG + Treg
Actc1 E99K + PBS
Actc1 E99K + Treg
2 mm
M) Apical fibrosis
% fibrosis in the apex
N) Left ventricular fibrosis
% fibrosis in left ventricle
Actc1: NTG E99K NTG E99K
Treg: - - + +

Figure 7. Ameliorated cardiac fibrosis and dysfunction following adoptive transfer of Tregs. Adoptive transfer of splenic Tregs (each with 200,000 cell per time, 1st intravascular injection at 25 weeks and 2nd one at 29 weeks of age) or PBS vehicle control were performed in *Rag-1*$^{\mathrm{KO}}$ or *Actc1*$^{\mathrm{E99K}}$ *Rag-1*$^{\mathrm{KO}}$ mice at 24 weeks-old for 8 weeks. Echocardiographic parameters including **(A)** EF% (n=7-11), **(B)** LVESV (n=7-11), **(C)** LVPW: d (n=7-11), and **(D)** LA size (n=3-9) are shown at 5 time points. **(E)** After 8 weeks, cardiac fibrosis was quantified using Picrosirius Red staining in **(F)** apical and **(G)** LV areas (n=4-8). Similarly, adoptive transfer of splenic Tregs (each with 200,000 cell per time, 1st intravascular injection at 37 weeks and 2nd one at 41 weeks of age) or PBS vehicle control was performed in *Actc1*$^{\mathrm{NTG}}$ and *Actc1*$^{\mathrm{E99K}}$ mice at 36 weeks-old for 8 weeks. Echocardiographic parameters including **(H)** EF% (n=3-6), **(I)** LVESV (n=3-6), **(J)** LVPW: d (n=3-6), and **(K)** LA size (n=3-6) are shown at 5 time points. **(L)** After 8 weeks, cardiac fibrosis was quantified using Picrosirius Red staining in **(M)** apical and **(N)** LV areas (n=4-8). Data are shown in mean ± SEM. Statistical analyses used two-way ANOVA with mixed-effects analysis: two-stage step-up method of Benjamini, Krieger and Yekutieli for echocardiographic parameters and one-way ANOVA with multiple comparison: Šidák for fibrosis (adjusted *p*-values: ∗: < 0.05, ∗∗: < 0.01, ∗∗∗: < 0.001, ∗∗∗∗: < 0.0001).

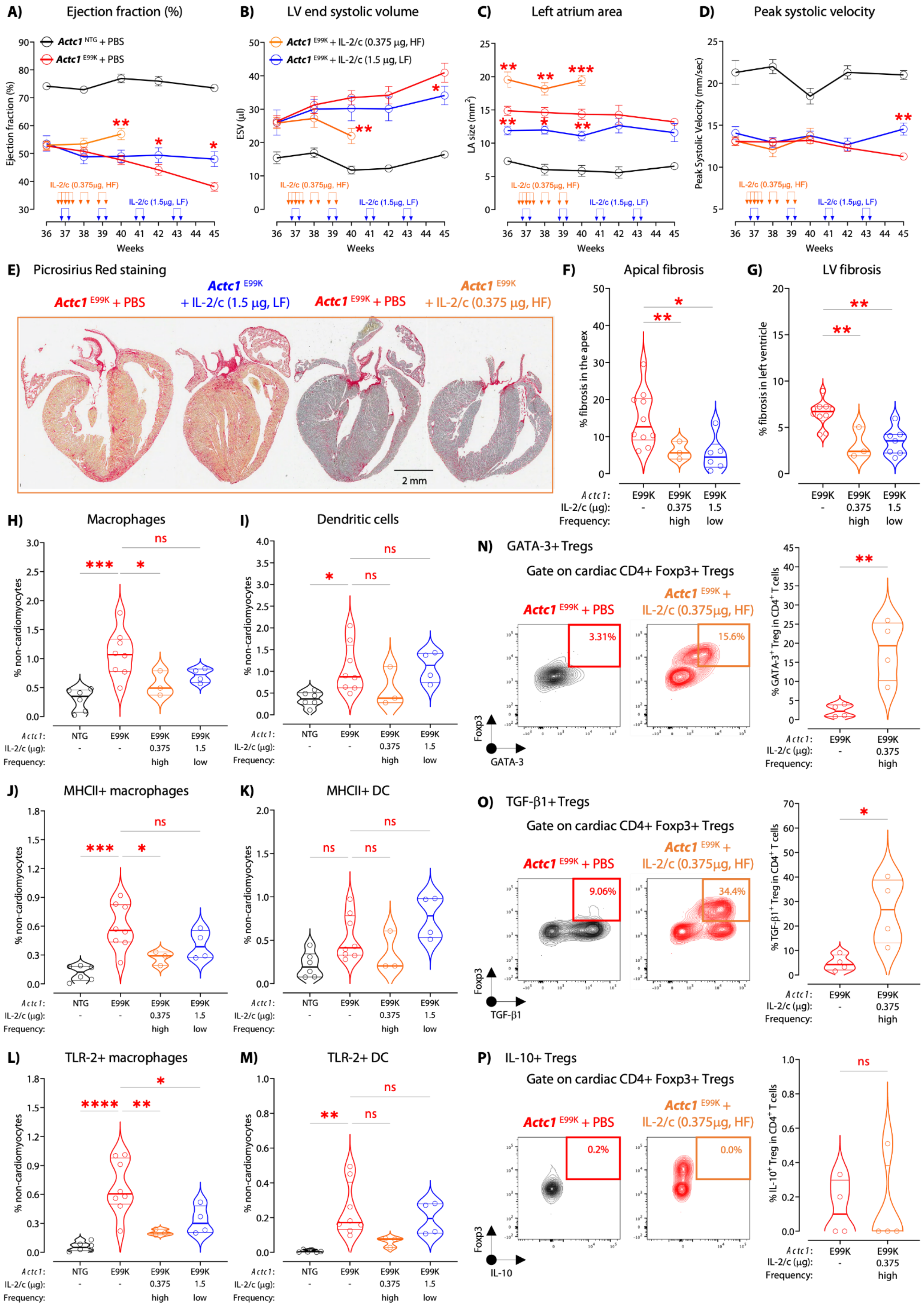
A) Ejection fraction (%)
Actc1 NTG + PBS
Actc1 E99K + PBS
Ejection fraction (%)
B) LV end systolic volume
Actc1 E99K + IL-2/c (0.375 µg, HF)
Actc1 E99K + IL-2/c (1.5 µg, LF)
ESV (µl)
C) Left atrium area
LA size (mm2)
D) Peak systolic velocity
Peak Systolic Velocity (mm/sec)
IL-2/c (0.375µg, HF)
IL-2/c (1.5µg, LF)
Weeks
36 37 38 39 40 41 42 43 44 45
E) Picrosirius Red staining
Actc1 E99K + PBS
Actc1 E99K + IL-2/c (1.5 µg, LF)
Actc1 E99K + PBS
Actc1 E99K + IL-2/c (0.375 µg, HF)
2 mm
F) Apical fibrosis
% fibrosis in the apex
G) LV fibrosis
% fibrosis in left ventricle
Actc1: E99K E99K E99K
IL-2/c (µg): - 0.375 1.5
Frequency: high low
H) Macrophages
I) Dendritic cells
% non-cardiomyocytes
Actc1: NTG E99K E99K E99K
IL-2/c (µg): - - 0.375 1.5
Frequency: high low
N) GATA-3+ Tregs
Gate on cardiac CD4+ Foxp3+ Tregs
Actc1 E99K + PBS
Actc1 E99K + IL-2/c (0.375µg, HF)
3.31%
15.6%
Foxp3
GATA-3
% GATA-3+ Treg in CD4+ T cells
Actc1: E99K E99K
IL-2/c (µg): - 0.375
Frequency: high
J) MHCII+ macrophages
K) MHCII+ DC
O) TGF-β1+ Tregs
9.06%
34.4%
TGF-β1
% TGF-β1+ Treg in CD4+ T cells
L) TLR-2+ macrophages
M) TLR-2+ DC
P) IL-10+ Tregs
0.2%
0.0%
IL-10
% IL-10+ Treg in CD4+ T cells
*
**
***
****
ns

Figure 8. Suppressed macrophage activation and limited fibrosis by IL-2 therapies. IL-2/c-induced Treg in vivo expansion in *Actc1*$^{\mathrm{E99K}}$ mice was performed using either high frequency (HF, 5 daily intraperitoneal injections at the first week followed by twice a week for two weeks) with very low dose (0.375 μg, n=10) or low-frequency (LF, twice intraperitoneal injections per week for every other week lasting for 8 weeks) with low dose (1.5 μg, n=11) regimens. Saline-treated *Actc1*$^{\mathrm{E99K}}$ (n=24) and *Actc1*$^{\mathrm{NTG}}$ mice (n=4) served as controls. Echocardiographic parameters (n=4-24) including **(A)** EF%, **(B)** LVESV, **(C)** LA size, and **(D)** peak systolic velocity (PSV) are shown at 3 or 5 time points. **(E)** After 8 weeks, cardiac fibrosis quantified using Picrosirius Red staining in **(F)** apical and **(G)** LV areas are shown (n=3-10). Flow cytometric analyses show the effects of IL-2/c regimens on the percentage of (**H)** macrophages and **(I)** DCs in the heart and their activation markers, including **(J-K)** MHCII+ and **(L-M)** TLR-2+ expression in macrophages and DCs, respectively (n=3-8). Percentage of **(N)** GATA-3^{+}, **(O)** TGF-β1^{+}, and **(P)** IL-10^{+} Foxp3^{+} Tregs in CD4^{+} T cells in *Actc1*$^{\mathrm{E99K}}$ hearts with or without high frequency IL-2/c regimen are shown with representative flow cytometric traces (n=4). Data are shown in mean ± SEM. Statistical analyses used unpaired t test for GATA-3^{+} and TGF-β1^{+} Tregs, Mann-Whitney test for IL-10^{+} Tregs, one-way ANOVA with multiple comparison: Šidák for macrophage and DC studies; one-way ANOVA with multiple comparison: two-stage step-up method of Benjamini, Krieger and Yekutieli for cardiac fibrosis; or two-way ANOVA with mixed-effects analysis: two-stage step-up method of Benjamini, Krieger and Yekutieli for echocardiographic parameters (adjusted p-values: $*$: < 0.05, $**$: < 0.01, $***$: < 0.001, $****$: < 0.0001).

Supplementary materials

Materials and Methods

In vivo cardiac phenotyping

Transthoracic echocardiography was performed on age and sex matched littermates under general anaesthesia (1 – 1.5% isoflurane) with a consistent heart rate around 480 bpm (± 20 bpm) using the Vevo 2100 or 3100 ultrasound system (Visalsonics) and a linear array MX550d transducer (22 to 55 MHz). Systolic function and left atrial size were measured from parasternal short-axis and long-axis images, respectively. For invasive phenotyping, mice were anaesthetized with isoflurane (1.25 – 1.5%) and a 1.4 F Mikro-tip catheter (Millar, SPR-671) was inserted into the left ventricle via the carotid artery for measuring hemodynamic indices. Data outside the heart rate range (480 ± 20 bpm) was excluded. Cardiac phenotyping was randomized, and data analysis was blindly conducted.

Flow cytometry for immune phenotyping

Murine hearts were perfused with cold 1 x Hanks' Balanced Salt Solution (HBSS) buffer (Life Technologies, 14065072) and cut into pieces before incubating with 5 ml 1 x HBSS buffer containing 300 U/ml collagenase II (Life Technologies, 17101015) and 10 U/ml DNase I (VWR, A3778.0500) in a C-tube (Miltenyi Biotec, 130-093-237) using a tailored digestion program on the gentleMACS Dissociator (Miltenyi Biotec, 130-093-235) for 45 minutes in a rolling station at 37°C. A clear cardiac single cell suspension in PBS containing 2 mM EDTA was achieved following a second programmed digestion, filtering large debris using 70 μm filters, and erythrocytes removal (BioLegend, 420302). Cells were then blocked with a cocktail of 2% mouse FcR blocker (Miltenyi Biotec, 130-092-575) and 10% rat (Life Technologies, 10710C), 10% rabbit (Life Technologies, 16120099) and 10% goat serum (Merck, G6767-100ML) in the Stain Buffer (BD Biosciences, 554656) at 4°C for 1 hour. A cocktail of fluorophore labelled primary antibodies was added with a brilliant staining buffer (BD Biosciences, 563794) to stain surface markers at 4°C for 1 hour. Samples were then fixed by the Fixation Buffer (BD

Biosciences, 554655) for 20 minutes and stored in FACS Stain Buffer at 4°C. Intracellular staining was performed using the eBioscience^{TM} Foxp3/Transcription Factor Staining Buffer Set (ThermoFisher, 00-5523-00). Samples were acquired using a BD Fortessa X-20 Analyzer and data were analyzed and illustrated using the FlowJo software (FlowJo^{TM} v10.8.1).

T cells were negatively selected from cardiac single cell suspension using the Pan T Cell Isolation Kit II, mouse (Miltenyi Biotec, 130-095-130) following manufacturer's instructions. Cardiac T cells were incubated with 1 x final concentration of Brefeldin A solution (Biolegend, 420601) at 37°C for 4 hours. Cells were further processed for FACS staining as described above.

Single-nucleus RNA-seq data analysis

Two publicly available snRNA-seq datasets were used in this study: i) LV samples from 15 late-stage patients with HCM and 16 non-failing (NF) individuals in a processed HDF5 format (*64*); ii) myectomy tissue from 10 mid-stage patients with HCM and 2 healthy donors, provided as a processed Seurat object (*65*). Both datasets were converted to an AnnData object for analysis in Python. Harmony v0.1 was employed to correct for potential batch effects between samples (*66*). Cell clustering was performed using the Leiden algorithm (*67*) in Scanpy v1.10.3 (*68*), followed by annotation based on marker genes. Differential gene expression analysis between HCM and controls were conducted within each cell type using a pseudo-bulk approach. Specifically, gene expression was aggregated per cell type within individuals, and a limma-voom model (limma v3.54.2) was applied (*69*). The model included age and sex as covariates for the late-stage samples ("expression ~ group + sex + age") and only group for the mid-stage samples ("expression ~ group, all males). Multiple testing correction was performed using the Benjamini-Hochberg method. GSEA was performed with fgsea v1.24.0 (*70*) against the hallmark gene sets from the Molecular Signatures Database (MSigDB) v2023.1 (*71, 72*). Terms with adjusted *p*-values < 0.05 were considered statistically significant.

Adoptive transfer of regulatory T cells

Splenocytes were isolated from *Foxp3*$^{\text{DTR-eGFP}}$ mice using the gentleMACS. Further enrichment of CD4$^+$ T cells was achieved with the mouse CD4$^+$ T cell Isolation Kit (Miltenyi Biotec, 130-104-454). The intrinsic GFP signal in Foxp3$^+$ Tregs was used to sort CD4$^+$ Foxp3$^+$ Tregs from CD4$^+$ Foxp3$^-$ T cells. Approximately 200,000 Tregs were then i.v. injected via the tail vein into a recipient mouse. This procedure was performed again 28 days later.

In vivo Tregs expansion induced by IL-2/anti-IL-2 complex

Recombinant mouse IL-2 (Bio-Techne, 402-ML-500/CF) was mixed with anti-IL-2 mAb (ThermoFisher Scientific, eBioscience$^{\text{TM}}$, JES6-1A12, 50 μg) to form an IL-2 complex (IL-2/c) at 4°C for one hour prior to each intraperitoneal injection. A time- and dose-dependent pilot study was performed to determine the optimal condition. As low dose IL-2/c caused VLS in *Actc1*$^{\text{E99K}}$ not *Actc1*$^{\text{NTG}}$ mice. With animal welfare consideration, we adopted two schemes for further experiments: i) high frequency (HF, five consecutive intraperitoneal injections in the first week followed by twice a week for two weeks) with very low dose (0.375 μg) and ii) low frequency (LF, two consecutive intraperitoneal injections every other week for eight weeks with low dose (1.5 μg).

Immunohistochemistry

For human heart samples, 3 mm tissue sections were mounted onto slides and immunostained on a Leica Bond Rx research stainer (Leica Biosystems), with the following antibodies, as per each antibody manufacturer's instructions: anti-CD11b (Abcam, ab52478, 1:1000 dilution), anti-CD3 (Leica Biosystems, CD3-565-L-CE, 1:500 dilution), and anti-CD68 (Abcam, ab783, 1:20 dilution). Following staining, images were captured by the Leica Biosystems anatomic pathology scanner and analysed using Aperio ImageScope 12.1 and FIJI software. In CD3$^+$ T cell staining, three samples of patients with HCM were excluded due to technical problems. In CD11b$^+$ myeloid cell staining, four healthy individuals and seven samples of patients with HCM were excluded due to sample accessibility or technical problems. In CD68$^+$ macrophage staining, two patients with HCM and one myocarditis patient sample were excluded due to technical problems.

Late gadolinium enhancement cardiac magnetic resonance (LGE-CMR) imaging

LGE MRI images for focal fibrosis assessment were acquired by the CMR specialists, who were kept unaware of mouse genotype, as described before (*73*): a segmented, double-gated, 3D inversion recovery (IR) gradient-echo pulse sequence (TR/TE = ~1000/1.3 ms) was used in short axis orientation with the following imaging parameters: FOV 30 x 30 mm^2, slab thickness 16 mm (covering the atria and ventricles); inversion time – 4 cardiac cycles (350 – 500 ms, depending on the heart rate); matrix size: 192 x 192 x 32; segment size: 8. Data acquisition commenced ~25 minutes post intraperitoneal Gd injections (100 µl Gadodiamide prepared at 0.5 mmol/kg; Omniscan, GE Healthcare/Amersham). Data were reconstructed offline and exported to TIFF for further analysis in Amira and FIJI.

Bulk RNA extraction and sequencing

Total RNA was extracted from snap frozen murine hearts using Rneasy Midi Kit (QIAGEN, 75144). Tissue was pulverized using mortar and pestle, an appropriate amount of RLT buffer was added, and tissue was homogenized by using 20-gauge needle fitted to an Rnase-free syringe. Contaminating proteins and DNAs were removed using proteinase K and RNAse free DNAse, respectively. RNA was eluted in a fresh collection tube with Rnase-free water. Total RNA was quantified using Quant-IT RiboGreen RNA Assay Kit (ThermoFisher Scientific, Invitrogen, R11490), and the integrity of RNA was assessed by a high sensitivity RNA ScreenTape (Agilent Technologies, 5067-5579). RNA integrity number estimates for all samples were over 8. Purification of mRNA, generation of double stranded cDNA and library construction were performed using NEBNext Ultra II Directional RNA Library Prep Kit for Illumina (New England Biolabs, E7760) with minor modifications to manufacturer specifications. Oligo d(T) beads were used to enrich mRNA with poly (A) tails. RNA was fragmented followed by first and second strand cDNA synthesis. Fragments were end repaired and A-tailed followed by adapter ligation. Finally, there was a USER-enzyme digestion and PCR enrichment step. Amplified libraries were analyzed for size distribution using the Agilent Tapestation 2200 D1000. Libraries were quantified using Picogreen and relative volumes were pooled accordingly. Sequencing was performed using the 150PE strategy on a NovaSeq6000 platform.

Bulk RNA-seq data processing

Reads were trimmed using CutAdapt v2.10 (*74*) and aligned to the mouse reference genome (GRCm39) using STAR v2.7.3a (*75*). Reads mapping to Ensembl-annotated genes were summarized using featureCounts v1.6.4 (*76*). The raw gene count matrix was imported into the R environment v4.1.0 (*77, 78*) for further processing and analysis with the edgeR package v3.40.2 (*79, 80*). Genes with very low expression were excluded based on the following heuristic: to be retained a gene needed to be expressed at the equivalent of 10 reads or more (after normalizing for library size) in at least as many samples as the smallest experimental group considered. The raw counts were then normalized using the trimmed mean of M values (TMM) method (*81*) in the edgeR package v3.40.2 (*79*) before transforming to z-scores to generate the corresponding heatmaps. Multiple testing correction was performed by using edgeR's default Benjamini-Hochburg method for controlling the false discovery rate. We performed (*82*) using fgsea v1.24.0 (*70*) with 1,000 permutations against the hallmark gene sets obtained from the Molecular Signatures Database (MsigDB) v2023.1 (*71, 72*). Terms with adjusted *p*-values < 0.05 were considered significant.

Single cell RNA-seq on mouse cardiac immune cells

Cell Isolation

Single cell suspension from *Actc1*$^{\mathrm{NTG}}$ and *Actc1*$^{\mathrm{E99K}}$ hearts (n=3, each) were prepared as mentioned before. Cells were then blocked for 1 hour at 4°C in blocking buffer cocktail as mentioned earlier, followed by labelling with an anti-mouse CD45 antibody (BioLegend, 103108, 1:1000) at 4°C for 1 hour. For multiplexing purposes, we employed a hashtag staining approach. Individual samples were stained with either TotalSeq-C0301 anti-mouse

Hashtag 1 Antibody: barcode – ACCCACCAGTAAGAC (BioLegend, 155861, 10 μg/ml per 10^6 cells), or TotalSeq-C0302 anti-mouse Hashtag 2 Antibody: barcode – GGTCGAGAGCATTCA (BioLegend, 155863, 10 μg/ml per 10^6 cells), or TotalSeq-C0303 anti-mouse Hashtag 3 Antibody: barcode – CTTGCCGCATGTCAT (BioLegend, 155865, 10 μg/ml per 10^6 cells) according to manufacturer's instruction. Cells from the same genotype were pooled and underwent sorting. Immune cells ($CD45^+$) were then sorted from total live cell population.

Library preparation

The densities of cell suspensions were determined with acridine orange/propidium iodide fluorescence using a LUNA-FX7 cell counter (Logos Biosystems). 14,000-30,000 cells per sample were loaded onto the 10X Genomics Chromium Controller (Chip K). Gene expression and feature barcoding libraries (CD45+ fractions) were prepared using the 10x Genomics Single Cell 5' Reagent Kits v2 (Dual Index) following manufacturer user guide (CG000330 Rev B). The final libraries were diluted to ~10nM for storage. The 10nM library was denatured and further diluted prior to loading on the NovaSeq6000 sequencing platform (Illumina, v1.5 chemistry, 150bp paired end).

Data analysis

Raw data were pre-processed using 10x Genomics cellRanger count v7.1.0 pipeline (*83*) with the mouse reference genome mm10 provided by 10x Genomics (version 2020-A). Then, ambient RNA was removed using SoupX v1.6.0 (*84*) and doublets were removed using DoubletFinder v2.0 (*85*) before being imported into Seurat v4.3.0 (*86*). The cells were filtered for mitochondrial genes (percent_mit < 20%), number of features/genes (500 < nFeature RNA < 5, 000), and ribosomal genes (percent_ribo < 20%). Samples were then integrated using harmony v0.1 (*66*). The cells were clustered by finding the variable features using FindVariableFeatures() function before using FindClusters() in Seurat v4.3.0 (*66*) before being annotated based on their marker genes using FindAllMarkers() function.

Histology

Mouse hearts were cannulated through the aorta, rinsed with ice cold 1 x HBSS followed with 4% paraformaldehyde (PFA) fixation overnight and then kept in 70% ethanol at 4°C. Hearts were cut through long axis into half and embedded in paraffin. For a general overview of cardiac morphology and fibrosis, 10 μm sections were stained with either Picrosirius Red (Polysciences, 24901-500) or Masson Trichrome Stain Kit (Polysciences, 25088-100), scanned with Aperio CS2 digital slide scanner (Leica Biosystems). Following Picrosirius red staining, images were captured using Aperio ImageScope 12.1 at consistent magnification levels for comparison between genotypes and across time points. Quantitative analysis was performed using ImageJ to assess fibrosis in defined regions as described before (*87*). The ventricle average included apex, left ventricle, septum, and right ventricle, while the atrium average included the left and right atrium. Wildtype hearts served as the baseline for threshold setting for each batch of staining.

Cardiac tissue cytokine and chemokine profiling

Protein extracts from cardiac tissue were homogenized using the Lysing Matrix D Tubes (MP Biomedicals, SKU:116913100) containing the RIPA lysis buffer with protease inhibitors and stored at -80°C. To measure cytokine and chemokine amounts, we employed the mouse V-PLEX Plus Pro-inflammatory Panel 1 and Cytokine panel 1 kits (Meso Scale Discovery, K15048D and K15245D, respectively) and followed manufacturer's recommended instructions. Briefly, two-fold diluted homogenized samples were added to the MSD assay plate pre-coated with antibodies of interest (1:40 dilution) and incubated for 2 hours at room temperature. Following 3 times of washing with PBS-T (0.5% Tween-20 in PBS), detection antibody (25 μl) as manufacturer instructed was then added and incubated for another 2 hours. After another washing step, MSD read buffer was added for plate reading using MSD SECTOR Imager SQ120 plate reader for further analysis. Using the MSD Discovery Workbench software, the data was collected and checked based on the overall average coefficient of variation

(CV). When CV value exceeds 20%, the data was excluded from analysis. To avoid batch variations, samples were normalised against the average value of 10 weeks-old wildtype samples.

Cell DIVE Imaging

To understand the distribution of cardiac immune cells, we employed the GE Cell DIVE system to image various cell types on formalin-fixed paraffin-embedded (FFPE) mouse heart tissue slides. The approach was described previously in FFPE human tissue samples (*88*). In brief, tissue slides were baked overnight at 60°C before transferred to xylene for de-waxing and rehydration using a gradient of ethanol solutions (from 100%, 95%, 70% to 50%). Each step was repeated twice for 5 minutes each followed by 2 washing with 1 x PBS. Slides were then permeabilized for 10 minutes in 0.3% Triton X-100 and washed once in 1 x PBS for 5 minutes.

Heat-induced epitope retrieval (HIER) steps were then conducted firstly in boiling a Citrate solution (Vector Labs, H3300, pH 6) and secondly in a Tris solution (Agilent, S1699, pH 9) for 20 minutes each in the NxGen decloaking chamber (Biocare Medical). This was followed by an additional cooling step for 10 minutes and 4 washing with 1 x PBS. Tissues were then blocked using 3% bovine serum albumin, BSA (Merck, A7906) and 10% donkey serum (Bio-Rad, C06SB) in 1 x PBS overnight. After one 1 x PBS washing, slides were exposed to an array of light emitting diodes (LEDs) for photo-irradiation and autofluorescence quenching in a black box for 12 hours. DAPI (Thermo, D3571) was then added for 15 minutes at room temperature. Following one 1 x PBS washing, Cell DIVE mounting media, made of 50% glycerol (Sigma, G5516) and 4% propyl gallate (Sigma, 2370), and cover slips were prepared for background imaging. A scan plan was acquired at 10X magnification to select regions of interest followed by imaging at 20X to acquire background autofluorescence in DAPI, FITC, Cy3 and Cy5 channels to generate virtual H&E images. Background imaging was used to subtract autofluorescence from all subsequent rounds of staining. Cover slips were removed in PBS and tissues were further blocked with mouse FcR blocking reagent (Miltenyi Biotec, 130-092-575, 1:10 dilution) for 1 hour at room temperature.

Each staining round allowed a mix of three primary antibodies prepared in blocking buffer overnight at 4°C (details are listed below). Unconjugated and conjugated primary antibodies were used in the first staining round, followed by three washing with 1 x PBS. The secondary antibodies including Donkey anti-goat IgG H&L AF555 (Abcam, ab150130, 1:1000) and Donkey anti-rabbit IgG H&L AF647 (Abcam, ab150075, 1:1000) were then incubated for 1 hour at room temperature. Conjugated primary antibodies were used in subsequent staining rounds with similar conditions. An antibody labelling kit was purchased (Invitrogen) to perform manual conjugation of some primary antibodies (in a BSA-AZIDE free format) with dyes in need.

Round1

SMA	ab5694	Abcam	Rabbit (CF450 kit)	5 µg/ml
CD45	AF114	biotechne	Goat	1:1000 dilution
FOXP3	D608R	CST	Rabbit (AF647 kit)	5 µg/ml

Round2

COLVI	ab200429	Abcam	Rabbit AF488	5 µg/ml
CD3	ab245731	Abcam	Rabbit (AF555 kit)	2 µg/ml
LY6G	1A8	Biolegend	Rat AF647	2.5 µg/ml

Bleaching of fluorophores between staining rounds was achieved using fresh prepared bleaching solution 0.1 M $NaHCO_3$ (Sigma, S6297, pH=11.2) and 3% H_2O_2 (Merck, 216763) for three times (15 minutes each) with one 1 x PBS washing for 1 minute in between bleaching rounds. Slides were then re-stained for DAPI for 2 minutes with one 1 x PBS washing for 5 minutes before imaging the dye-inactivated round as the new background round (for subsequent background subtraction). DAPI staining between imaging rounds assists in image registration and alignment. Slides were multiplexed with the next panel of three markers with iterative staining, bleaching, and imaging. A negative control slide stained with isotype-matched antibodies was used at the same concentration as the corresponding primary antibodies and using the same exposure settings. QuPath software 0.3 was used for visualization and the isotype controls were contrast-matched to sample stained with primary antibodies for comparison.

Confocal Imaging

Hearts from *Actc1*^{E99K} *Foxp3*$^{DTR/GFP}$ mice were dissected and perfused using cold 1 x HBSS buffer before a brief fixation step with 4% PFA for 1 hour at room temperature. Tissue samples were then incubated with 30% sucrose at 4°C overnight. Tissue-Plus O.C.T. compound (Agar Scientific, AGR1180) was added to a heart tissue containing mould within an ice-cold isopentane bath, which allows quick and smooth embedding process, and kept at -20°C until frozen sections using a cryostat. The cryosections were brought to room temperature and blocked with 3% BSA and 10% donkey serum at 4°C overnight. Slides were then incubated with mouse FcR blocker (Miltenyi Biotec; 130-092-575, 1:10 dilution) for 1 hour at room temperature and primary antibody against CD3 overnight at 4°C (Abcam ab245731, 2 μg/ml) followed by three PBS washes for 5 minutes each. Slides were mounted with Vectashield plus (cat:H-2000) containing DAPI and imaged with Zeiss LSM 900.

Supplementary figures

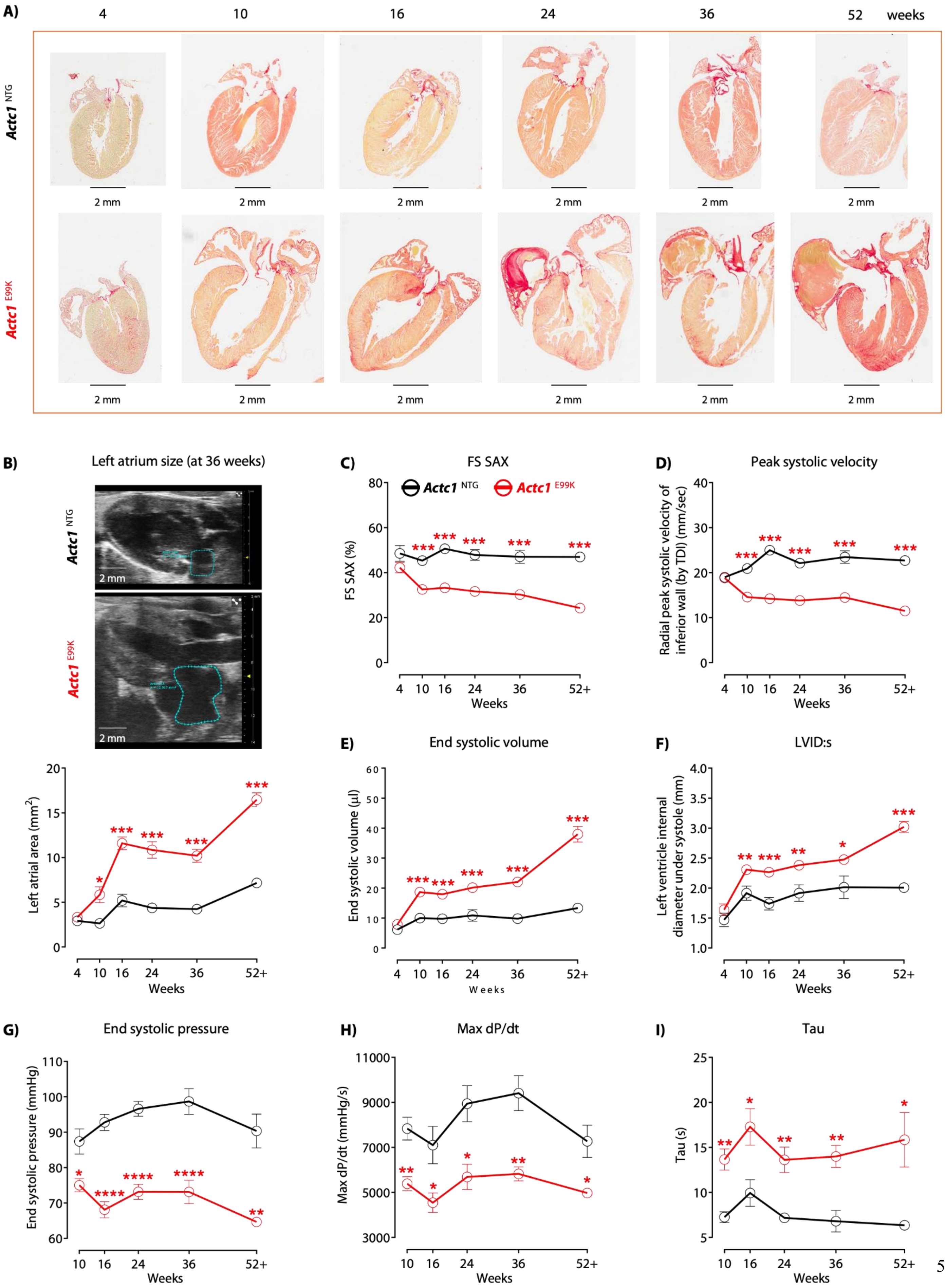
A)
4
10
16
24
36
52
weeks
Actc1 NTG
Actc1 E99K
2 mm
B)
Left atrium size (at 36 weeks)
Actc1 NTG
Actc1 E99K
2 mm
Left atrial area (mm²)
Weeks
C)
FS SAX
Actc1 NTG
Actc1 E99K
FS SAX (%)
Weeks
D)
Peak systolic velocity
Radial peak systolic velocity of inferior wall (by TDI) (mm/sec)
Weeks
E)
End systolic volume
End systolic volume (µl)
Weeks
F)
LVID:s
Left ventricle internal diameter under systole (mm)
Weeks
G)
End systolic pressure
End systolic pressure (mmHg)
Weeks
H)
Max dP/dt
Max dP/dt (mmHg/s)
Weeks
I)
Tau
Tau (s)
Weeks
4
10
16
24
36
52+
*
**
***
****

figure S1. A longitudinal study of cardiac dysfunction and fibrosis in *Actc1*$^{\mathbf{E99K}}$ mice. (A) Representative images in a long-axis view are shown to illustrate cardiac fibrosis stained with Picrosirius Red in *Actc1*$^{\mathrm{NTG}}$ and *Actc1*$^{\mathrm{E99K}}$ mice, aged from 4 to 52 weeks. Scale bar represents 2 mm. Echocardiographic parameters were analyzed by the Vevo Imaging software, including **(B)** LA size with representative images at 36 weeks of age ($n \geq 4$), **(C)** FS SAX ($n \geq 6$), **(D)** PSV ($n \geq 6$), **(E)** End systolic volume ($n \geq 6$), and **(F)** left ventricular internal dimension under systole ($n \geq 6$) from 4 to 52 weeks. Longitudinal haemodynamic studies show time-dependent changes in **(G)** end systolic pressure ($n \geq 4$), **(H)** Max dP/dt ($n \geq 4$), and **(I)** Tau ($n \geq 4$), from 10 to 52 weeks. Date are shown in mean ± SEM and statistical analyses were performed using two-way ANOVA with mixed-effects analysis: two-stage step-up method of Benjamini, Krieger and Yekutieli (adjusted *p*-values: $*$: < 0.05, $**$: < 0.01, $***$: < 0.001, and $****$: <0.0001).

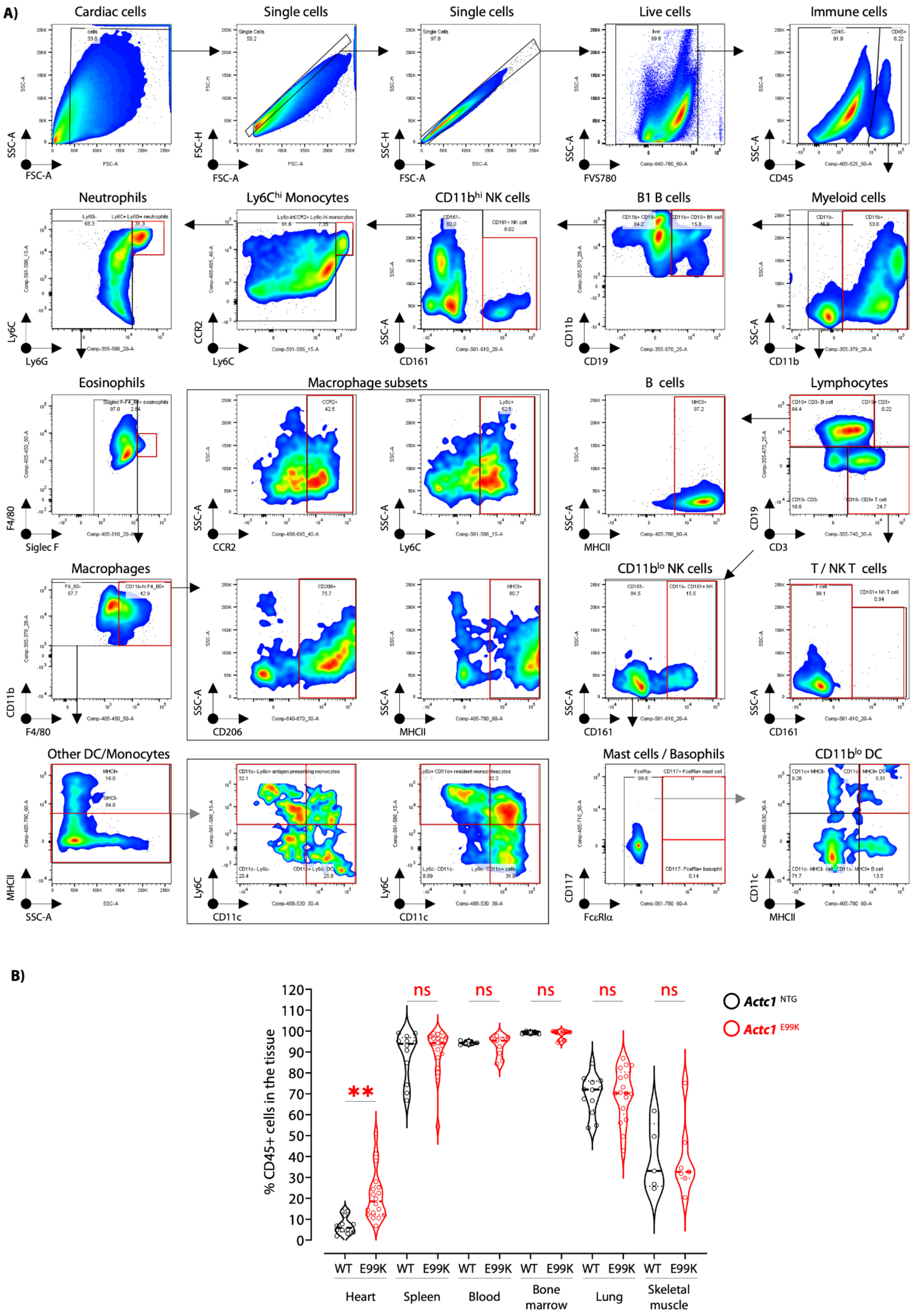
A)
Cardiac cells
Single cells
Single cells
Live cells
Immune cells
SSC-A
FSC-A
FSC-H
FSC-A
SSC-H
FSC-A
SSC-A
FVS780
SSC-A
CD45
Neutrophils
Ly6C^hi Monocytes
CD11b^hi NK cells
B1 B cells
Myeloid cells
Ly6C
Ly6G
CCR2
Ly6C
SSC-A
CD161
CD11b
CD19
SSC-A
CD11b
Eosinophils
Macrophage subsets
B cells
Lymphocytes
F4/80
Siglec F
SSC-A
CCR2
SSC-A
Ly6C
SSC-A
MHCII
CD19
CD3
Macrophages
CD11b^lo NK cells
T / NK T cells
CD11b
F4/80
SSC-A
CD206
SSC-A
MHCII
SSC-A
CD161
SSC-A
CD161
Other DC/Monocytes
Mast cells / Basophils
CD11b^lo DC
MHCII
SSC-A
Ly6C
CD11c
Ly6C
CD11c
CD117
FcεRIα
CD11c
MHCII
B)
% CD45+ cells in the tissue
120
110
100
90
80
70
60
50
40
30
20
10
0
**
ns
ns
ns
ns
ns
Actc1 NTG
Actc1 E99K
WT
E99K
Heart
Spleen
Blood
Bone marrow
Lung
Skeletal muscle

figure S2. Gating strategy of cardiac immune cell phenotyping using flow cytometry. (A) Gating strategy used to identify individual immune cell subsets is illustrated. **(B)** Percentages of CD45$^+$ immune cells in the heart (non-myocytes), spleen, blood, bone marrow, lung, and skeletal muscle from *Actc1*$^{\mathrm{NTG}}$ and *Actc1*$^{\mathrm{E99K}}$ mice at 52 weeks old are shown ($n \geq 5$). Data are shown in mean ± SEM and statistical analyses were performed using one-way ANOVA with multiple comparison analysis: Šidák (adjusted *p*-value: ∗∗: < 0.01).

A) Cardiac chemokine & cytokine gene expression

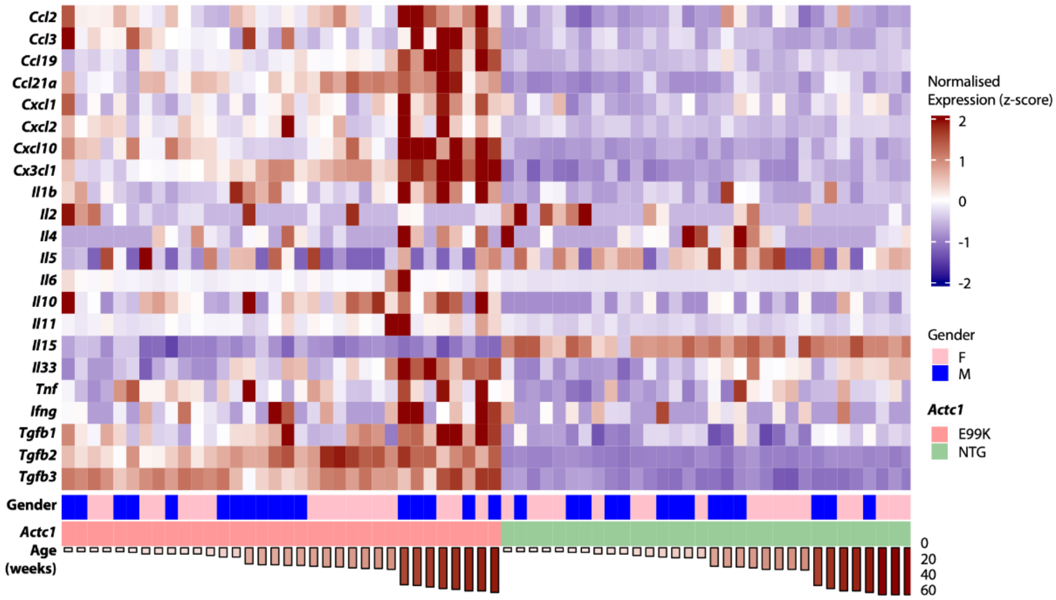

B) Cytokine and chemokine protein profiling in hearts

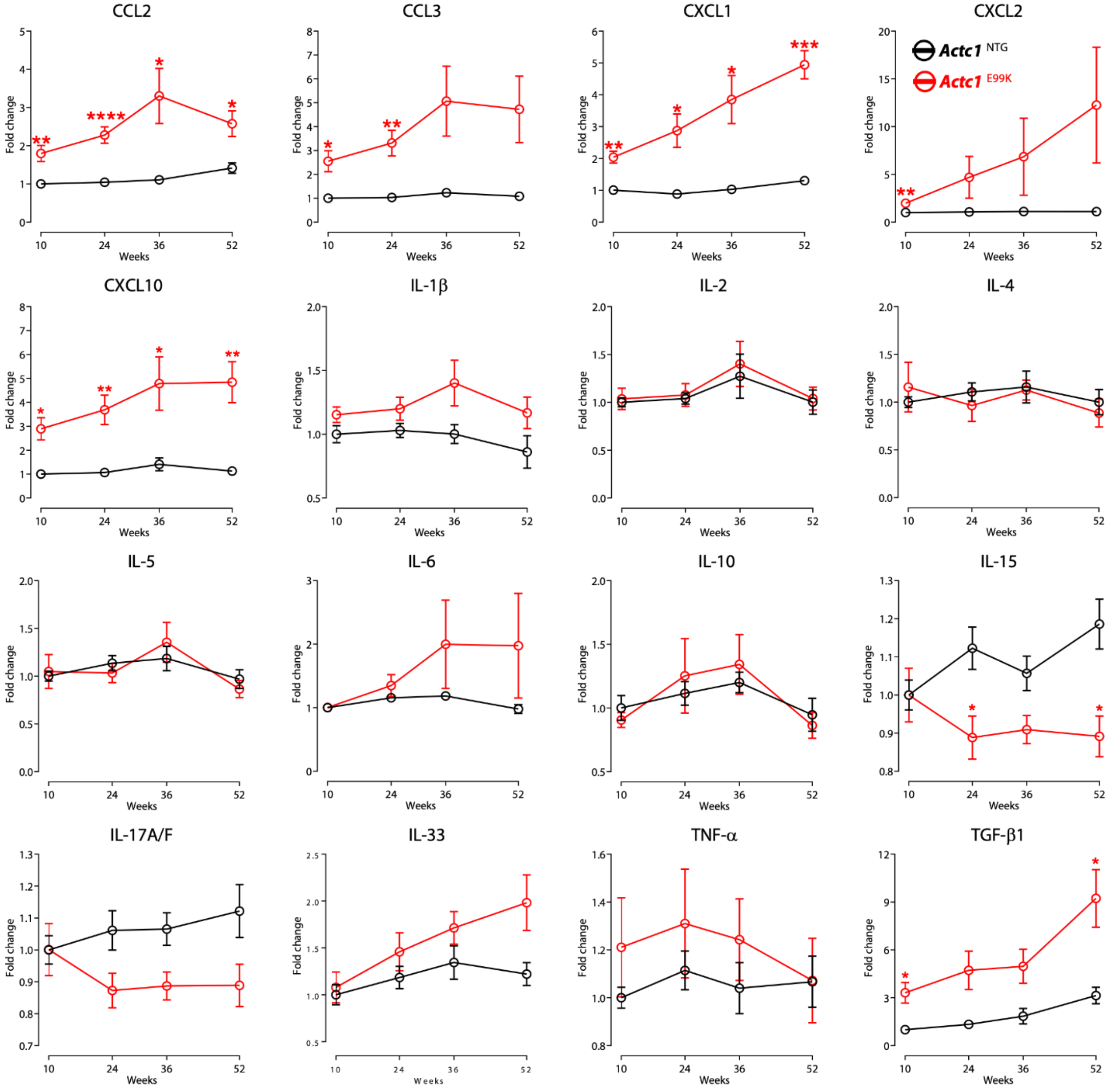

figure S3. Chemokine & cytokine gene and protein profiling in *Actc1*$^{\mathbf{E99K}}$ hearts. (A) Gene expression of key chemokines and cytokines in individual hearts from *Actc1*$^{\mathrm{NTG}}$ and *Actc1*$^{\mathrm{E99K}}$ mice are shown (n=3-4, per genotype per time point). Data are presented as Z-score heatmap, where darker red reflects stronger upregulation and darker blue reflects stronger downregulation. Gender (pink: females; blue: males), age (longer bar represents older age), and genotype (magenta: *Actc1*$^{\mathrm{E99K}}$; green: *Actc1*$^{\mathrm{NTG}}$) of individual mice are also shown. **(B)** Changes of key chemokines and cytokines at protein level in hearts from *Actc1*$^{\mathrm{NTG}}$ and *Actc1*$^{\mathrm{E99K}}$ are shown (n=8-11). Data are shown in mean ± SEM and statistical analyses were performed using two-way ANOVA mixed-effects analysis: two-stage step-up method of Benjamini, Krieger and Yekutieli (adjusted *p*-values: ∗: < 0.05, ∗∗: < 0.01, ∗∗∗: < 0.001, and ∗∗∗∗: < 0.0001).

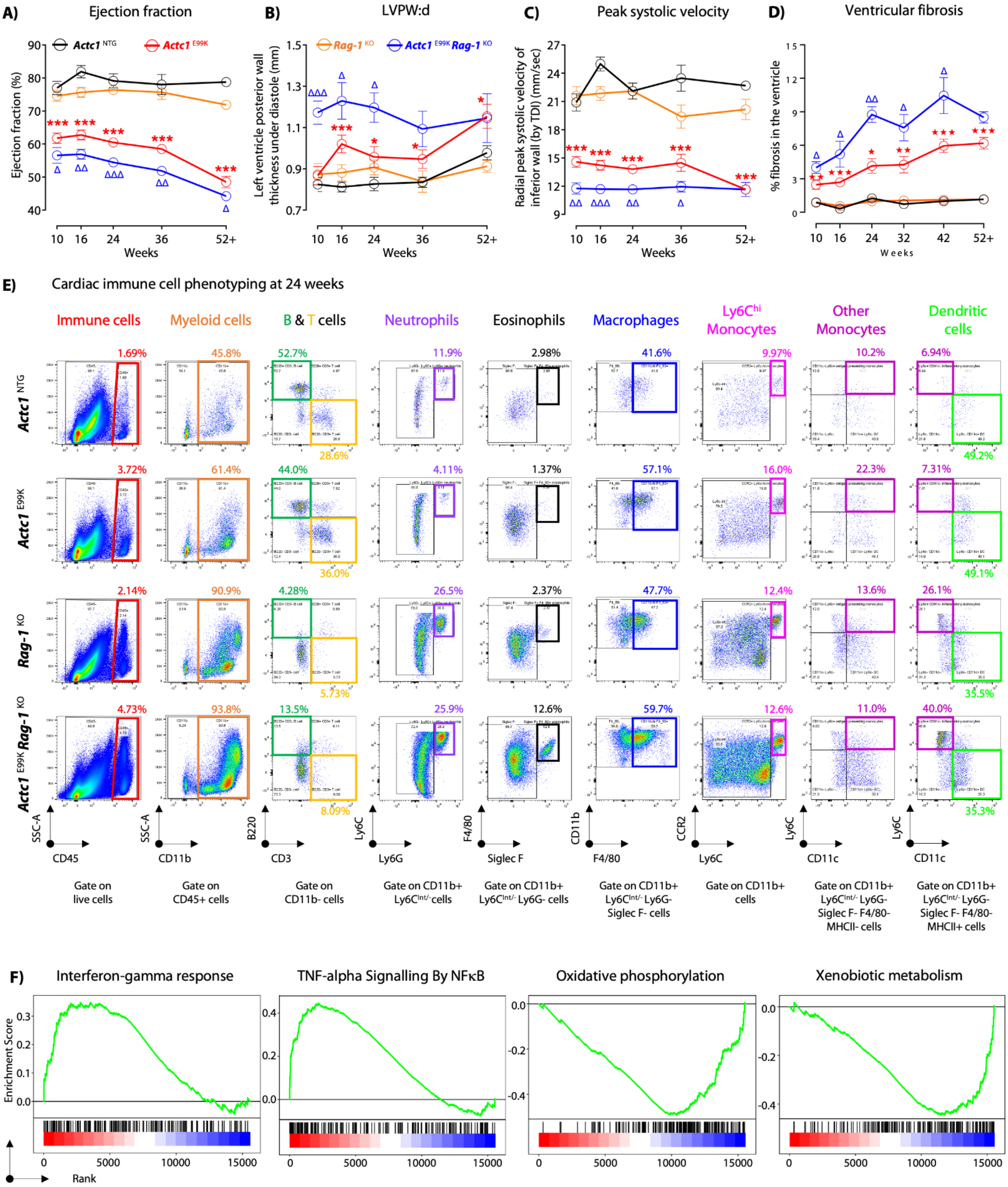
A)
Ejection fraction
Actc1 NTG
Actc1 E99K
Ejection fraction (%)
90
80
70
60
50
40
10 16 24 36 52+
Weeks
B)
LVPW:d
Rag-1 KO
Actc1 E99K Rag-1 KO
Left ventricle posterior wall thickness under diastole (mm)
1.5
1.3
1.1
0.9
0.7
10 16 24 36 52+
Weeks
C)
Peak systolic velocity
Radial peak systolic velocity of inferior wall (by TDI) (mm/sec)
27
24
21
18
15
12
9
10 16 24 36 52+
Weeks
D)
Ventricular fibrosis
% fibrosis in the ventricle
15
12
9
6
3
0
10 16 24 32 42 52+
Weeks
E)
Cardiac immune cell phenotyping at 24 weeks
Immune cells
Myeloid cells
B & T cells
Neutrophils
Eosinophils
Macrophages
Ly6Chi Monocytes
Other Monocytes
Dendritic cells
Actc1 NTG
1.69% 45.8% 52.7% 28.6% 11.9% 2.98% 41.6% 9.97% 10.2% 6.94% 49.2%
Actc1 E99K
3.72% 61.4% 44.0% 36.0% 4.11% 1.37% 57.1% 16.0% 22.3% 7.31% 49.1%
Rag-1 KO
2.14% 90.9% 4.28% 5.73% 26.5% 2.37% 47.7% 12.4% 13.6% 26.1% 35.5%
Actc1 E99K Rag-1 KO
4.73% 93.8% 13.5% 8.09% 25.9% 12.6% 59.7% 12.6% 11.0% 40.0% 35.3%
SSC-A CD45
SSC-A CD11b
B220 CD3
Ly6C Ly6G
F4/80 Siglec F
CD11b F4/80
CCR2 Ly6C
Ly6C CD11c
Ly6C CD11c
Gate on live cells
Gate on CD45+ cells
Gate on CD11b- cells
Gate on CD11b+ Ly6Cint/- cells
Gate on CD11b+ Ly6Cint/- Ly6G- cells
Gate on CD11b+ Ly6Cint/- Ly6G- Siglec F- cells
Gate on CD11b+ cells
Gate on CD11b+ Ly6Cint/- Ly6G- Siglec F- F4/80- MHCII- cells
Gate on CD11b+ Ly6Cint/- Ly6G- Siglec F- F4/80- MHCII+ cells
F)
Interferon-gamma response
TNF-alpha Signalling By NFκB
Oxidative phosphorylation
Xenobiotic metabolism
Enrichment Score
0.3
0.2
0.1
0.0
0.4
0.2
0.0
0.0
-0.2
-0.4
0.0
-0.2
-0.4
0 5000 10000 15000
Rank

figure S4. Cardiac and immune phenotyping of *Actc1*$^{\mathbf{E99K}}$ *Rag-1*$^{\mathbf{KO}}$ mice. Four groups of mice were studied, including *Actc1*$^{\mathrm{NTG}}$, *Actc1*$^{\mathrm{E99K}}$, *Rag-1*$^{\mathrm{KO}}$, and *Actc1*$^{\mathrm{E99K}}$ *Rag-1*$^{\mathrm{KO}}$. Echocardiographic parameters including **(A)** EF% (n≥5), **(B)** LVPW:d (n≥6), and **(C)** PSV (n≥7) are shown. **(D)** Time-dependent changes of ventricular fibrosis from 10 to 52+ weeks in four groups are shown (n=2-10). Data are shown in mean ± SEM and statistical analyses were performed using two-way ANOVA mixed-effects analysis: two-stage step-up method of Benjamini, Krieger and Yekutieli (adjusted *p*-values: ∗: < 0.05, ∗∗: < 0.01, and ∗∗∗: < 0.001) between *Actc1*$^{\mathrm{NTG}}$ and *Actc1*$^{\mathrm{E99K}}$. Additional pairwise comparison was made between *Actc1*$^{\mathrm{E99K}}$ and *Actc1*$^{\mathrm{E99K}}$ *Rag-1*$^{\mathrm{KO}}$ mice with illustrating adjusted *p*-values: "Δ": < 0.05, "ΔΔ": < 0.01, and "ΔΔΔ": < 0.001. **(E)** Representative flow cytometric traces and gating details of cardiac immune cell subsets in four groups at 24 weeks are presented (n=4). **(F)** Enrichment scores of four hallmark gene sets are shown between *Actc1*$^{\mathrm{E99K}}$ *Rag-1*$^{\mathrm{KO}}$ and *Actc1*$^{\mathrm{E99K}}$ hearts at 24 weeks (n=3-4).

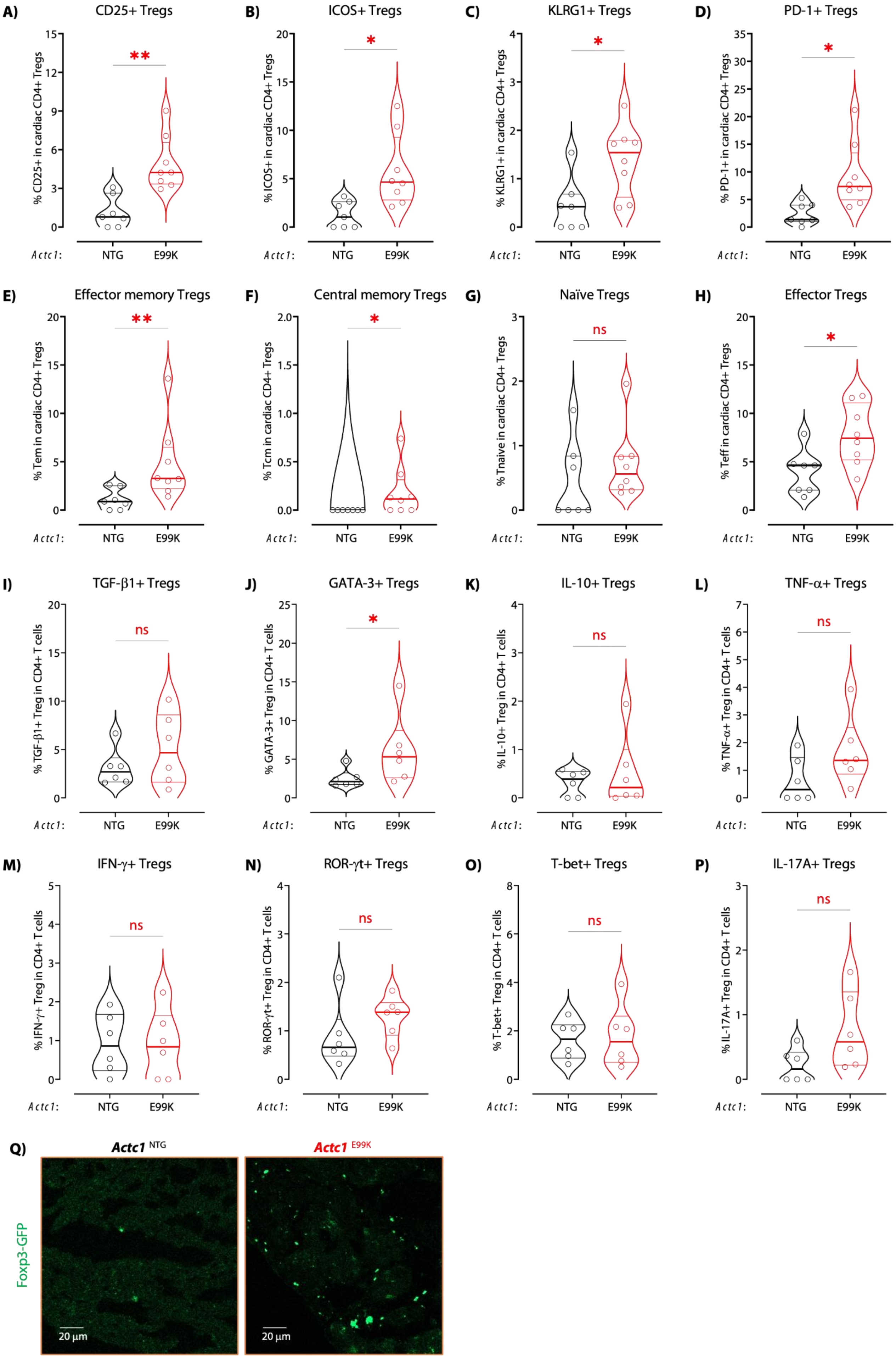
A)
CD25+ Tregs
% CD25+ in cardiac CD4+ Tregs
0
3
6
9
12
15
**
B)
ICOS+ Tregs
% ICOS+ in cardiac CD4+ Tregs
0
5
10
15
20
*
C)
KLRG1+ Tregs
% KLRG1+ in cardiac CD4+ Tregs
0
1
2
3
4
*
D)
PD-1+ Tregs
% PD-1+ in cardiac CD4+ Tregs
0
5
10
15
20
25
30
35
*
E)
Effector memory Tregs
% Tem in cardiac CD4+ Tregs
0
5
10
15
20
**
F)
Central memory Tregs
% Tcm in cardiac CD4+ Tregs
0.0
0.5
1.0
1.5
2.0
*
G)
Naïve Tregs
% Tnaive in cardiac CD4+ Tregs
0
1
2
3
ns
H)
Effector Tregs
% Teff in cardiac CD4+ Tregs
0
5
10
15
20
*
I)
TGF-β1+ Tregs
% TGF-β1+ Treg in CD4+ T cells
0
5
10
15
20
ns
J)
GATA-3+ Tregs
% GATA-3+ Treg in CD4+ T cells
0
5
10
15
20
25
*
K)
IL-10+ Tregs
% IL-10+ Treg in CD4+ T cells
0
1
2
3
4
ns
L)
TNF-α+ Tregs
% TNF-α+ Treg in CD4+ T cells
0
1
2
3
4
5
6
7
ns
M)
IFN-γ+ Tregs
% IFN-γ+ Treg in CD4+ T cells
0
1
2
3
4
5
ns
N)
ROR-γt+ Tregs
% ROR-γt+ Treg in CD4+ T cells
0
1
2
3
4
ns
O)
T-bet+ Tregs
% T-bet+ Treg in CD4+ T cells
0
2
4
6
8
ns
P)
IL-17A+ Tregs
% IL-17A+ Treg in CD4+ T cells
0
1
2
3
ns
Actc1:
NTG
E99K
Q)
Actc1 NTG
Actc1 E99K
Foxp3-GFP
20 µm
20 µm

figure S5. Presence of active CD4$^+$ Foxp3$^+$ Treg in *Actc1*$^{\mathrm{E99K}}$ hearts. Percentages of activation markers and inhibitory molecules in cardiac CD4$^+$ Foxp3$^+$ Tregs are shown, including **(A)** CD25, **(B)** ICOS, **(C)** KLRG1, **(D)** PD-1, **(E)** effect memory cells, **(F)** central memory cells, **(G)** naïve cells, and **(H)** effect cells, **(I)** TGF-β1, **(J)** GATA-3, **(K)** IL-10, **(L)** TNF-α, **(M)** IFN-γ, **(N)** ROR-γt, **(O)** T-bet, and **(P)** IL-17A (n=6-8). Data are shown in mean ± SEM and statistical analyses were performed using Mann-Whitney test (*p*-values: ∗: < 0.05, ∗∗: < 0.01, and ∗∗∗: < 0.001). **(Q)** Representative images of Foxp3+ Tregs with intrinsic GFP signals are shown in hearts from *Actc1*$^{\mathrm{NTG}}$ and *Actc1*$^{\mathrm{E99K}}$ mice. Scale bar represents 20 μm.

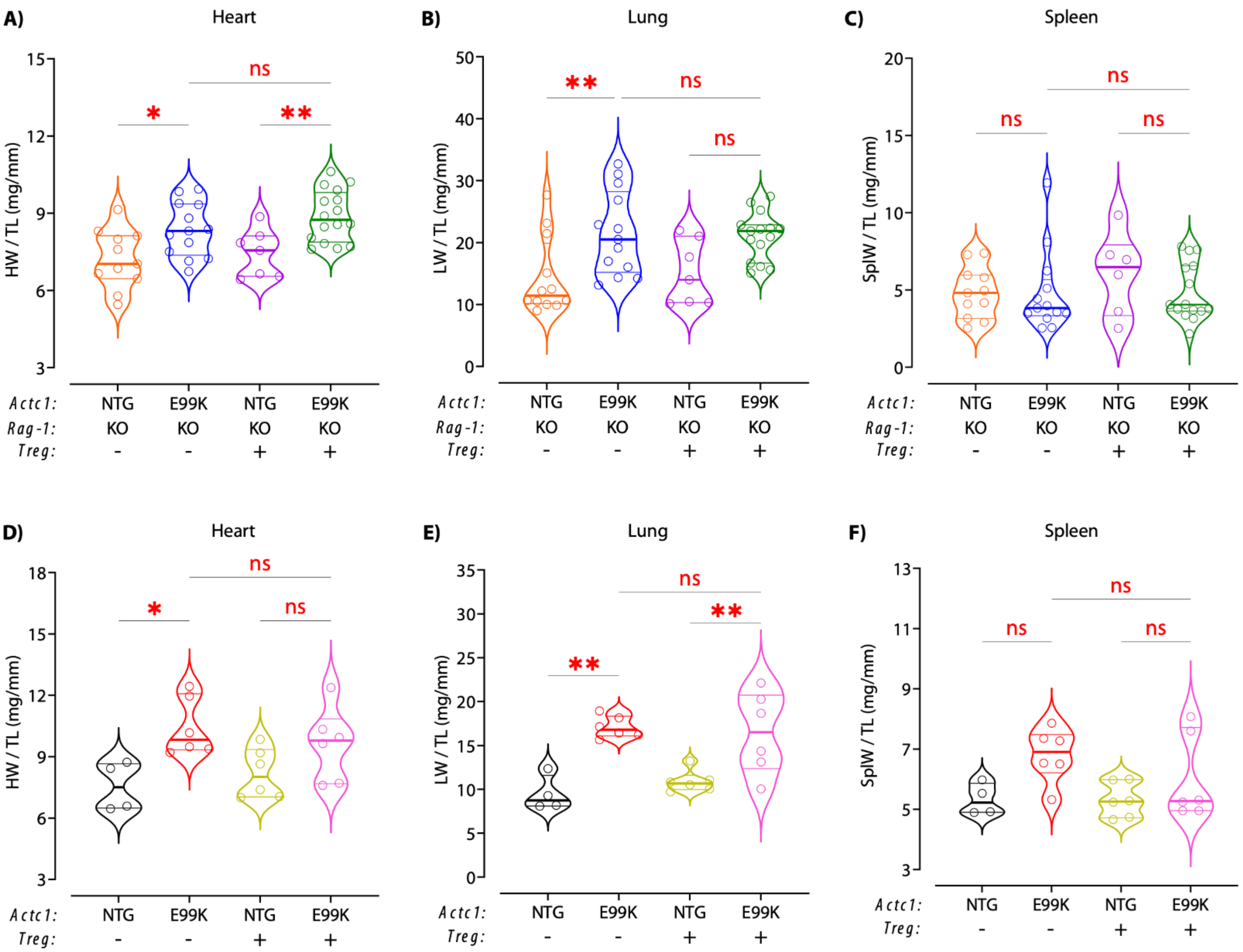

figure S6. The effect of Treg adoptive transfer on tissue remodelling. (A-C) The plots show the heart, lung, or spleen weight were normalized against tibia length following adoptive transfer of Tregs or PBS vehicle control in *Rag-1*$^{\text{KO}}$ and *Actc1*$^{\text{E99K}}$ *Rag-1*$^{\text{KO}}$ mice (n≥6). **(D-F)** The plots show the heart, lung, or spleen weight were normalized against tibia length following adoptive transfer of Tregs or PBS vehicle control in *Actc1*$^{\text{NTG}}$ and *Actc1*$^{\text{E99K}}$ mice (n≥6). Data are shown in mean ± SEM and statistical analyses were performed using one-way ANOVA multiple comparison analysis: Šidák (adjusted *p*-values: ∗: < 0.05, and ∗∗: < 0.01).

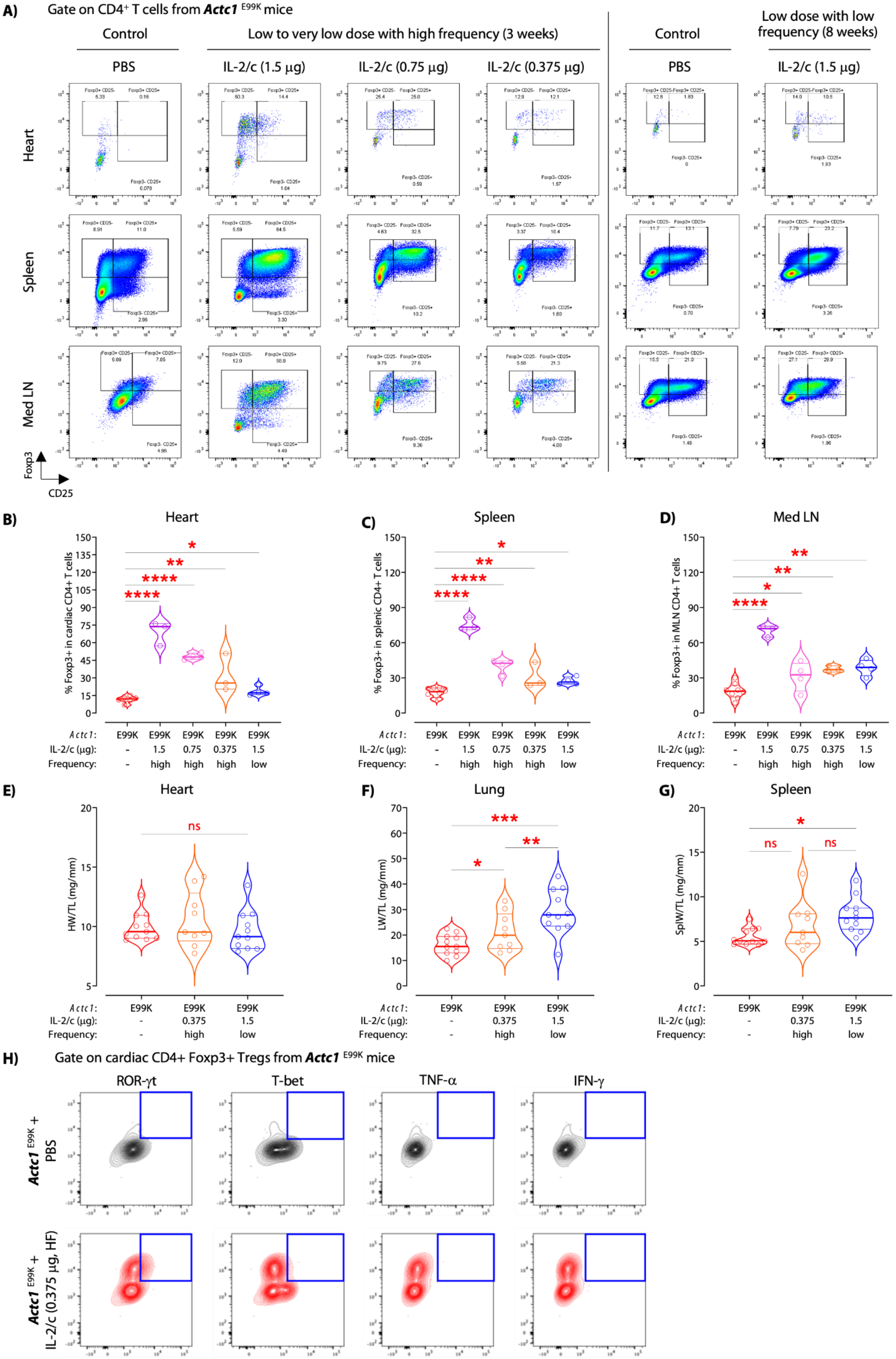
A)
Gate on CD4+ T cells from Actc1 E99K mice
Control
Low to very low dose with high frequency (3 weeks)
Control
Low dose with low frequency (8 weeks)
PBS
IL-2/c (1.5 μg)
IL-2/c (0.75 μg)
IL-2/c (0.375 μg)
PBS
IL-2/c (1.5 μg)
Heart
Spleen
Med LN
Foxp3
CD25
Foxp3+ CD25-
Foxp3+ CD25+
Foxp3- CD25+
B)
Heart
% Foxp3+ in cardiac CD4+ T cells
C)
Spleen
% Foxp3+ in splenic CD4+ T cells
D)
Med LN
% Foxp3+ in MLN CD4+ T cells
****
****
**
*
Actc1:
E99K
IL-2/c (μg):
-
1.5
0.75
0.375
1.5
Frequency:
-
high
high
high
low
E)
Heart
HW/TL (mg/mm)
ns
F)
Lung
LW/TL (mg/mm)
***
**
*
G)
Spleen
SplW/TL (mg/mm)
*
ns
ns
Actc1:
E99K
IL-2/c (μg):
-
0.375
1.5
Frequency:
-
high
low
H)
Gate on cardiac CD4+ Foxp3+ Tregs from Actc1 E99K mice
ROR-γt
T-bet
TNF-α
IFN-γ
Actc1 E99K + PBS
Actc1 E99K + IL-2/c (0.375 μg, HF)

figure S7. Time- and dose-dependent IL-2/c-induced Treg expansion in vivo. (A) Representative flow cytometric traces show duration-, frequency-, and dose-dependent changes of IL-2/c on Foxp3$^+$ and/or CD25$^+$ CD4$^+$ Treg expansion in the heart, spleen, and mediastinal lymph node (MLN). Percentages of Foxp3$^+$ Tregs in CD4$^+$ T cells are shown in **(B)** the heart (n=3-7), **(C)** spleen (n=3-7), and **(D)** MLN under various IL-2/c treatments (n=3-7). **(E-G)** Ratios of the heart, lung, and spleen weight against tibia length following IL-2/c-induced Treg expansion are shown (n=9-11). Data are shown in mean ± SEM and statistical analyses were performed using one-way ANOVA multiple comparison analysis: two-stage step-up method of Benjamini, Krieger and Yekutieli (adjusted *p*-values: ∗: < 0.05, and ∗∗: < 0.01, ∗∗∗: < 0.001, and ∗∗∗∗: < 0.0001). **(H)** Representative flow cytometric traces of several transcriptional factors and inflammatory cytokines expression in Foxp3$^+$ Tregs are shown in *Actc1*^{E99K} mice with or without high frequency IL-2/c treatment with very low dose (0.375µg).

Supplementary tables

Variables	**Diagnostic groups**			
	Normal (n=10)	**Myocarditis** (n=7)	**Heart failure** (n=6)	**HCM** (n=16)
Age (years), median (IQR)	34 (27 – 47)	55 (29 – 66)	71 (54 – 88)	58 (43 – 63)
Sex (male), n (%)	8 (72.7)	3 (42.9)	1 (16.7)	9 (52.9)
BMI (kg/m^2), median (IQR)	24 (19 – 28)	24 (23 – 28)	30 (24 – 32)	26 (22 – 30)
Co-morbidities, n (%)				
Hypertension	1 (10.0)	1 (14.3)	3 (50.0)	1 (6.3)
Ischaemic heart disease	0 (0)	0 (0)	2 (33.3)	1 (6.3)
Heart failure	0 (0)	0 (0)	6 (100)	7 (43.8)
Atrial fibrillation	0 (0)	1 (14.3)	1 (16.7)	5 (31.3)
Stroke	0 (0)	0 (0)	1 (33.3)	0 (0)
Diabetes mellitus type II	0 (0)	0 (0)	2 (33.3)	2 (12.5)
Heart weight (g), median (IQR)	364 (306 – 414)	490 (335 – 525)	448 (350 – 541)	549 (424 – 581)
Heart/body weight (g/kg), median (IQR)	4.8 (4.3 – 5.2)	5.4 (4.9 – 6.4)	5.6 (5.2 – 6.5)	6.7 (5.7 – 7.2)
Degree of fibrosis, n (%)				
Not significant	9 (90.0)	6 (85.7)	1 (16.7)	0 (0)
Mild	1 (10.0)	1 (14.3)	4 (66.6)	5 (31.3)
Moderate	0 (0)	0 (0)	1 (16.7)	6 (37.5)
Severe	0 (0)	0 (0)	0 (0)	5 (31.3)

BMI, body mass index; HCM, hypertrophic cardiomyopathy; IQR, interquartile range; Statistical significance was determined by *p*-values calculated using Ordinary one-way ANOVA.

Table S1. The baseline characterization of human heart samples in the study. Age, sex, body mass index (BMI), co-morbidities, heart weight, heart/body weight ratio, and degree of fibrosis are shown in healthy controls and individuals with myocarditis, heart failure, or HCM. Median values are shown for age, BMI, heart weight, and heart/body weight ratio with interquartile range (IQR) presented in the parentheses. Number of males, individual co-morbidities, and degree of fibrosis are shown with their percentages in total presented in the parentheses.

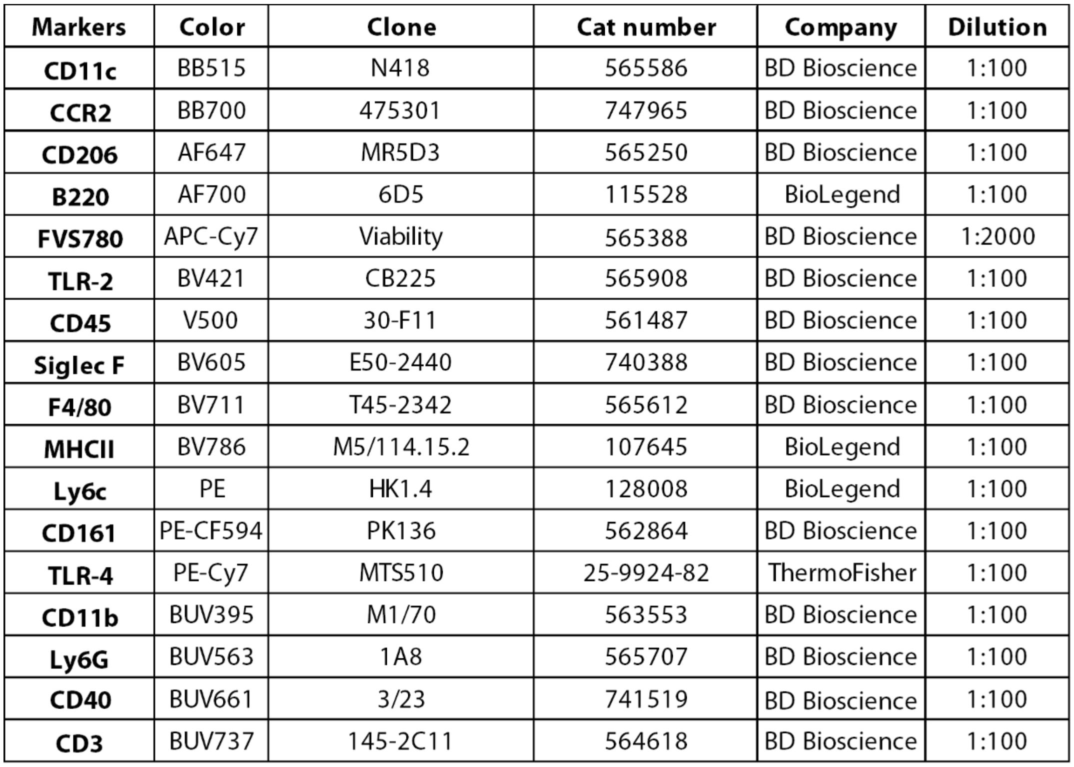

Markers	Color	Clone	Cat number	Company	Dilution
CD11c	BB515	N418	565586	BD Bioscience	1:100
CCR2	BB700	475301	747965	BD Bioscience	1:100
CD206	AF647	MR5D3	565250	BD Bioscience	1:100
B220	AF700	6D5	115528	BioLegend	1:100
FVS780	APC-Cy7	Viability	565388	BD Bioscience	1:2000
TLR-2	BV421	CB225	565908	BD Bioscience	1:100
CD45	V500	30-F11	561487	BD Bioscience	1:100
Siglec F	BV605	E50-2440	740388	BD Bioscience	1:100
F4/80	BV711	T45-2342	565612	BD Bioscience	1:100
MHCII	BV786	M5/114.15.2	107645	BioLegend	1:100
Ly6c	PE	HK1.4	128008	BioLegend	1:100
CD161	PE-CF594	PK136	562864	BD Bioscience	1:100
TLR-4	PE-Cy7	MTS510	25-9924-82	ThermoFisher	1:100
CD11b	BUV395	M1/70	563553	BD Bioscience	1:100
Ly6G	BUV563	1A8	565707	BD Bioscience	1:100
CD40	BUV661	3/23	741519	BD Bioscience	1:100
CD3	BUV737	145-2C11	564618	BD Bioscience	1:100

Table S2. The list of antibodies for all immune cell phenotyping using flow cytometry. Fluorescent dyes, clones, catalog numbers, and dilutions of individual antibodies against markers of live/dead, immune cell subsets and activation status are listed.

Markers	Colour	Clone	Cat Number	Company	Dilution
Foxp3	eGFP	Intrinsic signal			
GATA-3	BB700	L50-823	566642	BD Bioscience	1:100
IL-10	APC	JESS-16E3	554468	BD Bioscience	1:100
IL-17A	AF700	TC11-18H10	560820	BD Bioscience	1:100
CD8	APC-H7	53-6.7	560182	BD Bioscience	1:100
TGF-β1	BV421	TW7-16B4	141408	BioLegend	1:100
IFN-γ	BV480	XMG1.2	566097	BD Bioscience	1:100
FVS575V	BV605	Viability	565694	BD Bioscience	1:2000
IL-4	BV711	11B11	564005	BD Bioscience	1:100
TCR-β	BV786	H57-597	742484	BD Bioscience	1:100
ROR-γt	PE	Q31-378	562607	BD Bioscience	1:100
T-bet	PE-CF594	O4-46	562467	BD Bioscience	1:100
TNF-α	PE-Cy7	MP6-XT22	557644	BD Bioscience	1:100
CD4	BUV395	GK1.5	563790	BD Bioscience	1:100
TCR-γδ	BUV661	GL3	750410	BD Bioscience	1:100
CD335	BUV737	29A1.4	612805	BD Bioscience	1:100

Table S3. The list of antibodies for T cell phenotyping panel using flow cytometry. Fluorescent dyes, clones, catalog numbers, and dilutions of individual antibodies against markers of live/dead, T cell subsets with transcriptional factors and cytokines are listed. Foxp3+ Treg can be detected by its intrinsic GFP signal.

Supplementary data files

Data file S1. **Raw data and statistical methods for each figure.**

Data file S2. GSEA – all hallmark gene sets based on snRNA-seq data analysis of heart samples from mid-stage patients with HCM and healthy donors.

Data file S3. **GSEA – all hallmark gene sets based on snRNA-seq data analysis of heart samples from late-stage patients with HCM and non-failing individuals.**

Data file S4. **GSEA – significantly regulated hallmark gene sets based on bulk RNA-seq data analysis from the whole heart tissue from E99K mice from 5 to 60 weeks.**